minerals

MDPI

Article

Indium Mineralization in the Volcanic Dome-Hosted Ánimas–Chocaya–Siete Suyos Polymetallic Deposit, Potosí, Bolivia

Lisard Torró [1,*], Malena Cazorla [2], Joan Carles Melgarejo [2], Antoni Camprubí [3], Marta Tarrés [2], Laura Gemmrich [2], Marc Campeny [2,4], David Artiaga [2], Belén Torres [2], Álvaro Martínez [5], Diva Mollinedo [6], Pura Alfonso [7] and Osvaldo R. Arce-Burgoa [8,†]

[1] Geological Engineering Program, Faculty of Sciences and Engineering, Pontifical Catholic University of Peru (PUCP), Av. Universitaria 180, San Miguel, Lima 15088, Peru
[2] Departament de Mineralogia, Petrologia i Geologia Aplicada, Universitat de Barcelona (UB), C/ Martí i Franquès s/n, 08028 Barcelona, Spain; malecama.97@gmail.com (M.Caz.); joan.carles.melgarejo.draper@ub.edu (J.C.M.); martatm10@hotmail.com (M.T.); lauragemmrich.macia@gmail.com (L.G.); mcampenyc@bcn.cat (M.Cam.); dartiaga@ub.edu (D.A.); belentcgeo@gmail.com (B.T.)
[3] Instituto de Geología, Universidad Nacional Autónoma de México. Ciudad Universitaria, Coyoacán, CDMX 04510, Mexico; camprubitaga@gmail.com
[4] Departament de Mineralogia, Museu de Ciències Naturals de Barcelona, 08003 Barcelona, Spain
[5] Department of Earth Sciences, University of Geneva, Rue des Maraîchers 13, 1205 Geneva, Switzerland; alvaro@bizkaia.eu
[6] Facultad de Ciencias Geológicas, Universidad Mayor San Andrés, Av. Villazón N° 1995, Plaza del Bicentenario–Zona Central, La Paz, Bolivia; diva.moshi@gmail.com
[7] Departament d'Enginyeria Minera, Industrial i TIC, Universitat Politècnica de Catalunya, Av. de les Bases de Manresa 61-73, Manresa, 08242 Barcelona, Spain; maria.pura.alfonso@upc.edu
[8] Colegio de Geólogos de Bolivia, Edificio Señor de la Exaltación Nro. 4683, Av. Hernando Siles entre calles 1 y 2, Zona de Obrajes, Casilla 8941, La Paz, Bolivia; oarce.cgb@gmail.com
* Correspondence: lisardtorro@hotmail.com; Tel.: +51-912-617-691
† Current address: Eloro Resources Ltd. Av. La Floresta 497, Of. 101, San Borja, Lima 15037, Perú.

Received: 31 August 2019; Accepted: 29 September 2019; Published: 1 October 2019

Abstract: A volcanic dome complex of Miocene age hosts the In-bearing Ánimas–Chocaya–Siete Suyos district in SW Bolivia. Ore mineralization occurs as banded and massive infillings in sub-vertical, NE-SW striking veins. In this article, a detailed petrographic study is combined with *in situ* mineral geochemistry determinations in ore from the Arturo, Chorro and Diez veins in the Siete Suyos mine, the Ánimas, Burton, Colorada, and Rosario veins in the Ánimas mine and the Nueva vein in the Chocaya mine. A three-stage paragenetic sequence is roughly determined for all of them, and includes (1) an early low-sulfidation stage that is dominated by cassiterite, pyrrhotite, arsenopyrite, and high-Fe sphalerite (FeS > 21 mol. %); (2) a second intermediate-sulfidation stage dominated by pyrite + marcasite ± intermediate product, sphalerite (FeS < 21 mol. %), stannite, and local famatinite; and, (3) a late intermediate-sulfidation stage dominated by galena and Ag-Pb-Sn sulfosalts. Electron-probe microanalyses reveal high indium enrichment in stage-2 sphalerite (up to 9.66 wt.% In) and stannite (up to 4.11 wt.% In), and a moderate enrichment in rare wurtzite (up to 1.61 wt.% In), stage-1 sphalerite (0.35 wt.% In), cassiterite (up to 0.25 wt.% In_2O_3), and ramdohrite (up to 0.24 wt.% In). Therefore, the main indium mineralization in the district can be associated to the second, intermediate-sulfidation stage, chiefly in those veins in which sphalerite and stannite are more abundant. Atomic concentrations of In and Cu in sphalerite yield a positive correlation at Cu/In = 1 that agrees with a $(Cu^{+} + In^{3+}) \leftrightarrow 2Zn^{2+}$ coupled substitution. The availability of Cu in the mineralizing fluids during the crystallization of sphalerite is, in consequence, essential for the incorporation of indium in its crystal lattice and would control the distribution of indium

enrichment at different scales. The highest concentrations of indium in sphalerite, which is found in the Diez vein in the Siete Suyos mine, occur in crustiform bands of sphalerite with local "chalcopyrite disease" texture, which has not been observed in the other studied veins. In stannite, the atomic concentrations of In are negatively correlated with those of Cu and Sn at Cu + In = 2 and Sn + In = 1. Thus, atomic proportions and correlations suggest the contextualization of the main indium mineralization in the sphalerite–stannite–roquesite pseudoternary system.

Keywords: critical metals; high-tech metals; indium; sphalerite; Bolivian-type deposits

1. Introduction

The high-tech metal indium (In) is classified as a critical raw material due to its high economic importance and elevated risk of supply [1–10]. In nature, this metal mostly occurs in the crystal lattice of base-metal sulfides and oxides in substitution of cations with similar radii (i.e., Zn, Fe, Cu, Sn, As) and only a few, and rare, discrete indium minerals have been defined [11–14]. High concentrations of In have been described in sphalerite, cassiterite, chalcopyrite, stannite, tennantite, and tin sulfosalts [14]. Indium is not exploited as a primary commodity, but rather as a co-product or by-product of base metals, chiefly in zinc [15–19], but also in tin [20] and copper [21] ores.

The occurrence of In is reported in ore deposits that span a broad range of ages and mineralization styles [11,14]. High concentrations are described prominently in exhalative deposits hosted in volcanic (e.g., [22,23]) and sedimentary sequences (e.g., [24]), granite-hosted (including greisen-type, e.g., [25,26]), vein-stockwork Sn-W, porphyry Sn and xenothermal Sn-W-Cu-Zn-Pb-Ag veins (e.g., [27–30]), skarn (e.g., [18,31]), ,and epithermal (e.g., [15,16,32,33]) deposits.

A number of polymetallic mineral deposits from the central Andes in Peru, Bolivia, and northern Argentina are listed as major In hosts [11,34,35]. Chief among them are xenothermal polymetallic-vein deposits hosted by the Andean tin belt [29,36–39]. Whole-rock geochemical analysis of ore samples (including composites) from SW Bolivia deposits has revealed In contents as high as 5740 ppm for Potosí, 3080 ppm for Huari Huari, 2730 ppm for Bolivar, and 2510 ppm for Ánimas-Siete Suyos deposits [37]. Ishihara et al. [37], by means of electron microprobe analyses (EPMA) on one sample from the Potosí deposit, determined that "black sphalerite" is the major host for In (up to 1.27 wt.%) and it occurs along with local "petrukite-bearing zones". A femto-second laser ablation inductively coupled plasma mass spectrometry (fs-LA-ICP-MS) study combined with EPMA by Murakami and Ishihara [29] yielded concentrations of In as high as 7.89 wt.% in Fe-rich ("black") sphalerite in a sample from the Huari Huari deposit, and concentrations up to 5.08 wt.% In in a sample from the Potosí deposit; in addition, these authors determined concentrations up to 18 wt.% In in an undetermined Zn-In mineral. In the Santa Fe mining district, the contents of In in ore are up to 200 ppm and concentrations of In as high as 2.03 wt.% In were determined in sakuraiite [38]. In the Huari Huari deposit, an EPMA study that is based on a large number of ore samples distributed along the mineralized zones allowed for Torró et al. [39] to determine that an early generation of sphalerite rich in Cu, and in part co-crystallized with stannite, was the main host for In, and pointed out that the highest concentrations of this metal are found in a central position of the deposit complex.

Although the In-bearing Ánimas–Chocaya–Siete Suyos district (also referred to as Chocaya or Gran Chocaya district) is not considered of world-class significance, it was regarded by Ahlfeld and Schneider-Scherbina [40] as the southernmost large Bolivian tin deposit. Tin was indeed the main commodity that was mined in the district until the 1950s, when lead and silver became the main products. Being discovered in 1800, the beginnings of large-scale mining in this district are intimately linked to the name of two of the so-called tin barons in Bolivia, Avelino Aramayo, and Simón I. Patiño. The Ánimas mine was first exploited by the Aramayo Mines Company from 1870. The Chocaya (or Chocaya La Vieja) mine was first mined by the Minera y Agrícola Oploca Company (Santiago de Chile, Chile; which in 1926 became part of the Patiño Group) since 1884. Both of the companies were nationalized in 1952 and were renamed as Telamayu and Santa Ana, and they belong to the

Corporación Minera de Bolivia (COMIBOL). Since the early 1990s to this day, mines in the district are operated by mining cooperatives mostly for lead, zinc, and silver.

In this work, we present in situ chemical analyses of ore minerals from the In-bearing Ánimas–Chocaya–Siete Suyos district. Such chemical determinations are systematically linked to petrographic observations and contextualized along thorough paragenetic sequences built for selected veins. By doing so, we seek a better understanding of the temporal and spatial distribution of In in xenothermal deposits hosted in volcanic-dome complexes following a similar research scheme as Torró et al. [39] did for the Huari Huari sediment-hosted polymetallic vein deposit. The results of this research should serve as a basis for the exploration of In in other xenothermal vein deposits, in particular those that are hosted in volcanic-dome complexes, and they might be of help for the optimization of metallurgical flowsheets for ore processing with economic concentrations in this metal. This article corresponds to a group of papers of various Bolivian tin deposits with the same collective aim [33,39–41].

2. Geologic Setting

2.1. Geodynamic Setting

The highlands of the Andes cover about one-third of the Bolivian territory, with the remaining two-thirds being covered by tropical lowlands. In Bolivia, the Andean Cordillera splits into two parallel mountain chains, the Western and Eastern Cordilleras, which are separated by the Altiplano (i.e., the high plains between 3600 and 4500 m above the sea level) [40,42–46]. The geology of both Cordilleras is contrasting. The Eastern Cordillera is composed of a pile of thrusted, folded and variably metamorphosed marine Paleozoic and both marine and non-marine Cretaceous sedimentary rocks that underwent deformation during the Caledonian (Ordovician), Hercynian (Devonian to Triassic), and Andean (Cretaceous to Cenozoic) orogenic cycles [45]. The restricted outcrops of igneous rocks of variable ages occur throughout the Eastern Cordillera [47,48]. In stark contrast, the Western Cordillera is mostly composed of late Miocene to Recent intermediate (andesitic and dacitic) volcanic rocks that intruded and overlaid Jurassic and Cretaceous sedimentary and volcanic rocks. On the one hand, Cenozoic igneous rocks in the Altiplano and Western Cordillera are described to record a high mantle input and belong to the I-type, magnetite-series. Igneous rocks in the Eastern Cordillera, on the other hand, mostly resulted from sediment melting in a thickened continental crust, have peraluminous, reduced signatures, and belong to the S-type, ilmenite-series [47,49,50]. The third of the physiographic units of the Andes in Bolivia, the Altiplano, is an internally drained basin that contains a thick succession of sedimentary rocks derived from both Cordilleras since the Upper Cretaceous [51]. The maximum width of the Altiplano (that is, the maximum separation between the Cordilleras in surface; ~300 km) occurs in the so-called "elbow of the Andes", which is also known as the Bolivian orocline or Arica Deflection [52]. North of the orocline, the Andes run NW-SE, whereas south of the orocline they run N-S.

The general geology and the metallogeny of the Central Andes have both been controlled by a quasi-continuous subduction along the western margin of the South American plate over the last ca. 250 M.y. [53–59]. Several Paleogene and Neogene polymetallic mineralized belts juxtapose to morphotectonic provinces in the Andean orogen [56,59]. The Andean tin belt, in which the studied deposit is located, is confined to the Eastern Cordillera through Bolivia with short extensions into southern Peru and northern Argentina [40,45,56,60–62]. Mineralization in the Andean tin belt is genetically connected to reduced, peraluminous magmas of mostly late Oligocene to Miocene ages, although a late Triassic-early Jurassic mineralization episode is described in NW Bolivia, north of the Bolivian orocline [56,63–65]. Age aside, there are marked differences in the mineralization styles and depths of emplacement along the tin belt north and south of the Bolivian orocline. North of the orocline, the Sn-W mineralization forms veins within granite batholiths or at their contacts with sedimentary hosts. South of the orocline, Sn, Sn-W, and Sn-polymetallic mineralizations are "shallower" and related to porphyritic intrusions, dome complexes, hydrothermal breccia pipes, and

collapse calderas. These eventually developed advanced argillic lithocaps within the epithermal environment over high-grade mesothermal (or xenothermal [60]) vein deposits [61,63,66–68].

2.2. Geology of the Deposit

The Ánimas–Chocaya–Siete Suyos district is located in the Potosí Department, 150 km south of the city of Potosí and near the town of Atocha at altitudes between 4150 and 4300 m.a.s.l. Approximate coordinates of the main mines are 20°57'51" S 66°18'24" W for the Ánimas mine, 20°57'6" S 66°17'43" W for the Siete Suyos mine, and 20°58'29" S 66°19'51" W for the Chocaya mine. Physiographycally, this district sits on the western flank of the Eastern Cordillera, close to the triple junction that is drawn by the Eastern Cordillera, the Western Cordillera, and the southern end of the Altiplano (Figure 1). The district is included in the Quechisla mining group [61] within the Andean (or Bolivian) tin belt (Figure 1).

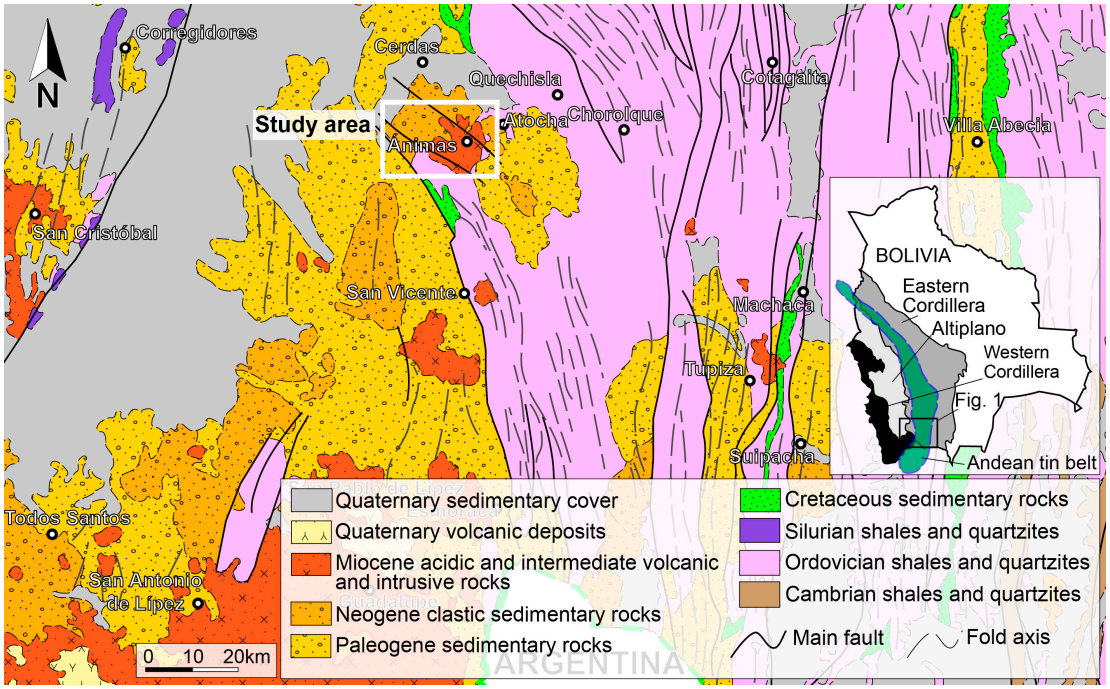

Figure 1. Regional geological map showing the location of the study area (Ánimas-Chocaya-Siete Suyos district; white box). Inset shows the location of the map within the Western Cordillera (Andean morphotectonic units are after Arce-Burgoa [61]).

Mineralization in the Ánimas–Chocaya–Siete Suyos district is genetically associated with the Chocaya volcanic caldera complex, which is about 9 km in diameter and Miocene in age [40,60,61]. A pile of lava and pyroclastic deposits of dacitic composition is protruded by a central dome of the same composition (Figure 2). The volcanic complex is hosted by Ordovician sandstones and slates, which are faulted and folded along successive close anticline and syncline structures with NW-SE striking axial planes [69]. In the area of study, Ordovician rocks are unconformably overlain by gently dipping interbedded sandstones and tuffs of the Quehua Formation, of Oligocene-Miocene age [69–72]. Ordovician and Quehua Formation series were both intruded and covered by effusive and explosive deposits associated to the Chocaya volcanic caldera system (Figure 2A) [60,61,69]. Dacite lavas show porphyritic textures described by subhedral quartz, plagioclase, biotite, sanidine, and augite phenocrysts (and lesser amounts of hornblende and hypersthene) in a fine-grained groundmass of the same composition [69].

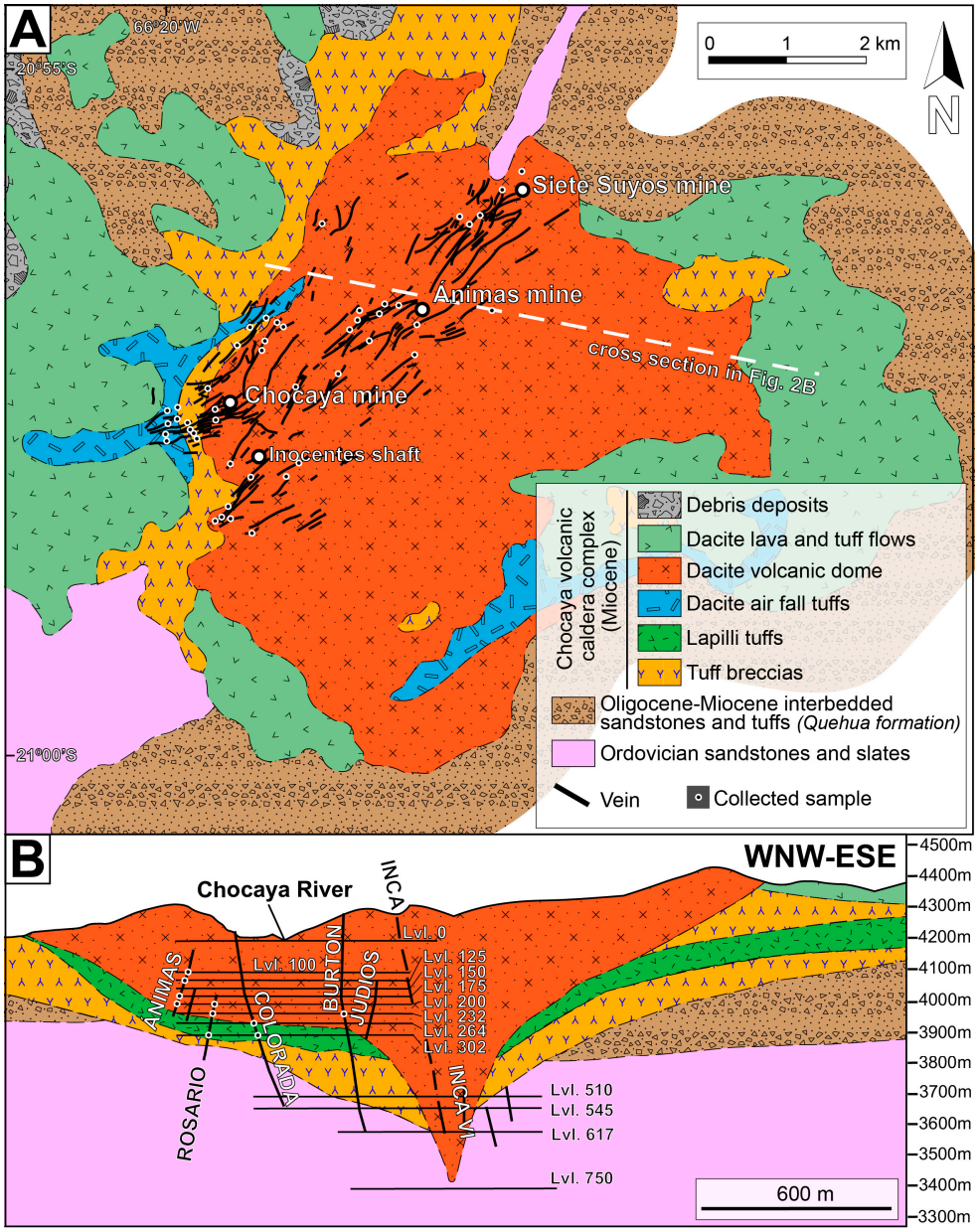

Figure 2. (**A**) Geological map showing the distribution of veins in the Ánimas–Siete Suyos–Chocaya mining district. The location of this map is shown in Figure 1. (**B**) Conceptual geologic model of the Ánimas–Siete Suyos–Chocaya deposit. The trace of the cross section on surface is shown in (**A**). Modified from Arce-Burgoa [61]. Lvl. = level.

Mineralization and hydrothermal alteration affected both volcanic complex and Ordovician host rocks. Hydrothermally altered rocks extend across over 8 km² (surface projection), thus forming an irregular NE-SW belt [60,69]. Hydrothermal alteration is more pervasive in rocks of the Chocaya volcanic complex, chiefly in the basal tuff breccia (Figure 2B), and it is poorly developed in Ordovician rocks, probably due to their nearly non-reactive character with hydrothermal fluids. Intense quartz-sericite (fine-grained muscovite) and local quartz-tourmaline assemblages grade outward to less pervasive quartz-sericite and, further, to propylitic (mostly chlorite) assemblages. Nevertheless, local shallow quartz-kaolinite assemblages are described in the Siete Suyos and Ánimas mines [69]. In general, such distribution of hydrothermal alteration assemblages fits that of mesothermal tin deposits underlying advanced argillic (epithermal) lithocaps in the Bolivian tin belt

[67]. Reported K-Ar ages in the area are 13.8 ± 0.2 Ma (unweighted mean value) for biotite grains from unaltered volcanic rocks, and of 12.5 ± 0.2 Ma for a sericitized sample (whole-rock age) [73].

Volcanic and basement metamorphosed sedimentary rocks are crosscut by a NE-SW striking network of steeply-dipping veins that extends for over 5 km between the Siete Suyos (to the NE) and Chocaya mines (to the SW; Figure 2A) [60,61,69,74]. The main veins in the Siete Suyos mine are named Esperanza, San Patricio, Salvadora, Arturo, Diez, Nueva, Colorada, and Inca (1 to 7) and they have been worked from level 0 at 4202 m.a.s.l. to level 28 at 3564 m.a.s.l. The Colorada and Inca veins extend into the Ánimas mine (Figure 2A). In addition to these, important veins in the Ánimas mine also include the Ánimas, Rosario and Burton veins—the latter being formerly considered the Ag- and Pb-richest vein in Bolivia [40]. Some of them are exploited at depth intervals of ~900 m (e.g., Burton and Colorada veins; Figure 2B) between the surface and level 780, at 3407 m.a.s.l. (note that the name of the levels differs for the Ánimas and Siete Suyos mines, so that, for example, level 19 in the Siete Suyos mine is at the same topographic elevation as level 302 in the Ánimas mine). The longest of these veins is Colorada, which extends for over 2450 m along strike. In the Chocaya mine, the main veins are named Inocentes, Nueva, San Bartolomé, and Candelaria, among which Nueva is the longest as it extends about 770 m along strike and more than 150 m in depth. Noteworthy, single veins in the three mines are often hosted by both Ordovician (lower segment of the vein) and volcanic complex (upper segment of the vein) rocks (Figure 2B).

Buerger and Maury [74] and Sugaki et al. [69] noted contrasting metalliferous contents for veins along the Ánimas–Chocaya–Siete Suyos district. In the Siete Suyos mine, Sugaki et al. [69] described that both veins were largely composed of cassiterite and pyrite (Colorada, Inca, and Nueva) and veins that consisted mostly of pyrite, sphalerite, stannite and galena, with lesser amounts of cassiterite (Esperanza, Salvadora, Arturo, and Diez). In contrast, the ore mineral assemblages described in veins from the Ánimas mine are dominated by sulfides (chiefly sphalerite, pyrite, wurtzite, galena) and contain only minor amounts of cassiterite, except for the Colorada vein (which is cassiterite-rich). Ore mineral assemblages in veins from the Chocaya mine are dominated by sphalerite, wurtzite, galena, pyrite, and silver-antimony sulfosalts. According to Sugaki et al. [69], the described ore mineral assemblages depict a metalliferous concentric zoning with (1) a NE-SW trending ellipsoidal core rich in Sn, which contains the Colorada, Inca and Nueva veins in the Siete Suyos mine and their extensions into the Ánimas mine; (2) an intermediate zone that surrounds this core, which is centered in the Ánimas mine and enriched in Zn, Ag and, to a lesser extent, in Sn; and (3) a farther, external zone centered in the Chocaya mine that is rich in Ag, Zn and Pb. Homogenization temperatures (T_h) and salinities of fluid inclusions in vein quartz along the district exhibit significant differences, perhaps in association with the metalliferous zoning: higher values are reported in the Sn-rich core (T_h: 220 to 360 °C; 4.6 to 11.9 wt.% NaCl equiv.) than in the intermediate (T_h: 170 to 270 °C; 3.8 to 4.9 wt.% NaCl equiv.) and external (T_h: 170 to 270 °C; 3.7 to 5.2 wt.% NaCl equiv.) zones [69].

3. Materials and Methods

The study area is comprised within the quadrangle defined by coordinates 20°55′50″ S 66°20′30″ W and 20°59′20″ S 66°17′12″ W. The study is based on 82 rock samples from the Ánimas–Siete Suyos–Chocaya district, including in situ surface (n = 50) and mining gallery (underground; n = 32) samples. Studied samples are representative of the different metalliferous domains defined by Sugaki et al. [69] in the Ánimas (n = 35), Siete Suyos (n = 24), and Chocaya (n = 23) mine areas. Sampled veins in mine galleries include Ánimas (levels 100, 125, 175, and 200), Arturo (levels 19, 20, and 21), Burton (level 232), Chorro (levels 14 and 16), Colorada (levels 264 and 302), Diez (level 15), Jalisco (level 75), Nueva (level 125), and Rosario (levels 175, 200, 232, 302). The availability of underground samples for each vein has been restricted to active galleries at the time of each sampling campaign during 2012, 2015, and 2018. As a consequence, for example, no samples from veins at mine levels below the 302 level in the Chocaya and Ánimas mines (Figure 2B) are available in this study, as the respective galleries have been flooded for decades. This study also includes mineralogical and geochemical data on two underground samples from the Siete Suyos mine area that were picked up from pre-feed stockpiles and whose allocation to a particular vein and the level is unknown. A list of the samples,

the mine from which they were sampled and their geographic (coordinates) or relative (vein and gallery level) location is given in Table S1 in Supplementary Material.

The samples were prepared as polished thick (n = 58) and thin (n = 3) sections for their study under the optical microscope using reflected and transmitted light. A selection of these samples was examined on an environmental SEM Thermo Fisher Quanta 650 FEI equipment with an EDAX-Octane Pro EDS microanalysis system that is available at Centro de Caracterización de Materiales of the Pontifical Catholic University of Peru (CAM-PUCP). The operating conditions were 20 keV accelerating voltage and 5 nA in backscattered electron (BSE) mode.

Mineral chemistry analyses of sulfide minerals were performed on 58 polished sections while using five-channel JEOL JXA-8230 electron microprobe equipment (Jeol Ltd., Tokyo, Japan) available at Centres Científics i Tecnològics of the Univeristy of Barcelona (CCiT-UB), operated at 20 kV acceleration voltage, 20 nA beam current and with a beam diameter of 5 μm. Analytical standards and lines used for analyses were: sphalerite (Zn, *K*α), chalcopyrite (Cu, *K*α), FeS_2 (Fe and S, *K*α), Ag (Ag, *L*α), Sb (Sb, *L*α), Bi (Bi, *M*β), CdS (Cd, *L*β), PbS (Pb, *M*α), GaAs (As, *L*α), Sn (Sn, *L*α), InSb (In, *L*α) Ge (Ge, *L*α), and Ta (Ta, *L*β). The detection limits (d.l.) for each element, representative analyses of the different minerals investigated, and the normalization constants used for formula calculations are shown in Table S2 in Supplementary Material.

Mineralogical determinations were also carried out by means of X-ray Diffraction (XRD; n = 8). The samples were ground in an agate mortar and were manually pressed by means of a glass plate to obtain a flat surface in cylindrical standard sample holders of 16 mm diameter and 2.5 mm height. The diffractograms were obtained in a Bruker D8 Discover powder diffractometer in Bragg-Brentano θ/2θ geometry of 240 mm of radius, nickel filtered Cu *K*α radiation (k = 1.5418 Å), and 45 kV–40 mA at the CAM-PUCP. The software PANalytical X'Pert Highscore© 2.0.1 (Version 2.0.1, PANalytical, Almelo, The Netherlands) was used to subtract the background of the patterns, to detect the peaks, and to assign mineral phases to each peak.

4. Mineralogy and Textures

4.1. Siete Suyos Mine

The mineralogy and micro-textures of the Arturo, Chorro and Diez veins in the Ánimas mine are described below.

The Arturo vein is mostly composed of sulfides, between which sphalerite is the most abundant, and quartz. Sphalerite flooded the central portion of the vein and the interstitial space in the anhedral pyrite, arsenopyrite, cassiterite, and quartz association that rims the vein (Figure 3A–E). Pyrite occurs as grains with sizes between some tens of micrometers and 0.5 mm, and it shows evidence for extensive corrosion, such as engulfment and secondary porosity, which are lined with sphalerite and quartz (Figure 3A–C). A few pyrite grains preserve straight faces that recall pseudo-hexagonal shapes of the crystals previous to their corrosion and replacement; trails of micrometer-sized inclusions that are roughly parallel to crystal faces that reproduce hexagonal patterns are relatively common (Figure 3B,C). Cassiterite is a relatively minor phase in the Arturo vein and occurs as anhedral grains of less than 100 μm across that have been extensively replaced by sphalerite (Figure 3D–G); they are often intergrown with pyrite and quartz (Figure 3F,G). Arsenopyrite is even scarcer than cassiterite and it has been extensively replaced by pyrite and sphalerite, thus emphasizing its early precipitation (Figure 3G). Traces of galena are observed filling porosity within and as thin veinlets across pyrite and sphalerite (Figure 3E,I). Additionally, filling porosity, mostly within sphalerite, are trace amounts of sulfosalts, which include fizélyite [$Ag_5Pb_{14}Sb_{21}S_{48}$], owyheeite [$Ag_{3+x}Pb_{10-2x}Sb_{11+x}S_{28}$, $-0.13 < x > +0.20$], miargyrite [$AgSbS_2$], pyrargyrite [Ag_3SbS_3], diaphorite [$Ag_3Pb_2Sb_3S_8$], and hocartite [$Ag_2(Fe^{2+},Zn)SnS_4$], either as monomineralic or polymineralic infillings (Figure 3H,I). In polymineralic infillings, miargyrite is veined by fizélyite (Figure 3H) and galena, diaphorite and pyrargyrite were replaced by hocartite (Figure 3I).

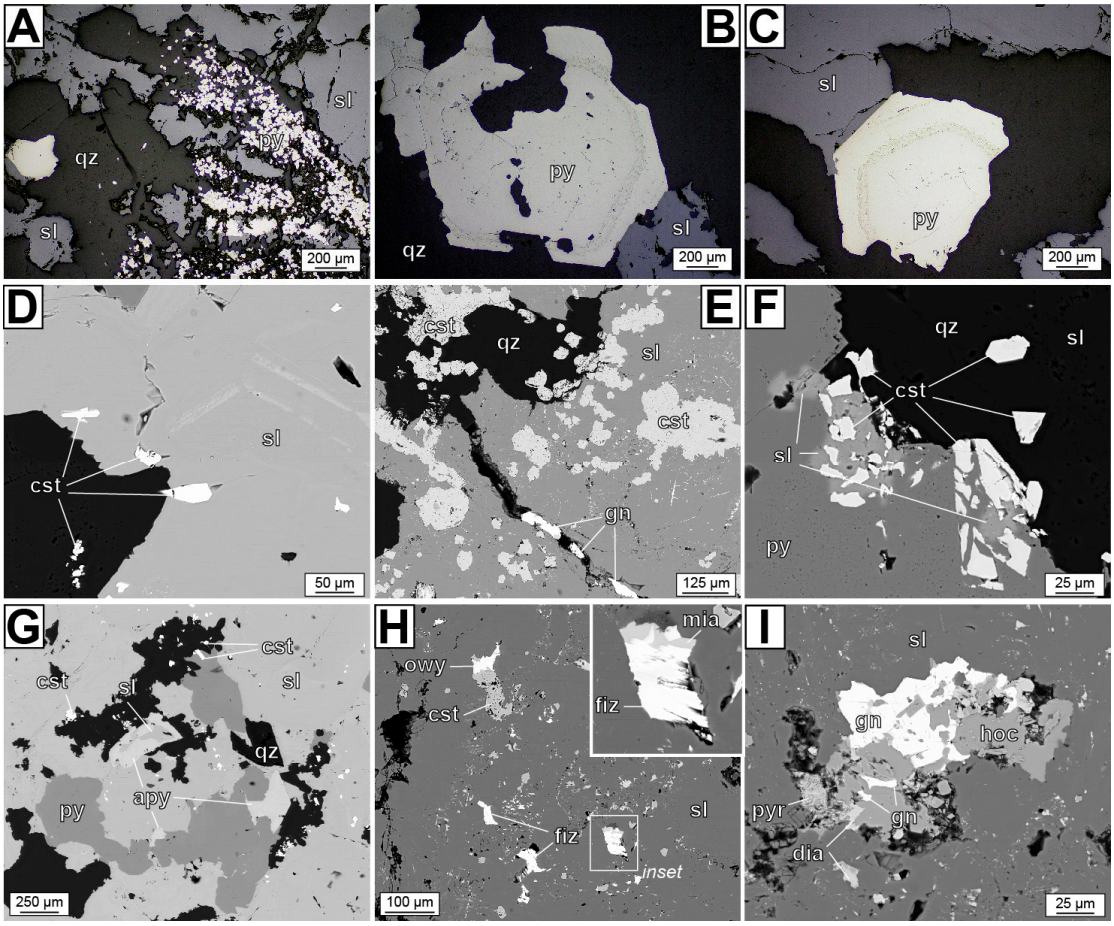

Figure 3. Photomicrographs (reflected light; **A**–**C**) and back-scattered electron images (**D**–**I**) of textural features in the Arturo vein in the Siete Suyos mine. (**A**) General aspect of the mineralization at the Arturo vein, with anhedral pyrite crystals within a groundmass of sphalerite and quartz. (**B**) Corroded pyrite grain that shows conspicuous engulfment and secondary porosity; some of the straight (not corroded) crystal faces and the arrangement of micrometer-sized porosity draw a pseudo-hexagonal shape. (**C**) Corroded pyrite grain with trails of micrometer-sized porosity parallel to the crystal faces before corrosion. (**D**) Minute cassiterite relicts within a sphalerite groundmass; note the compositional zoning in sphalerite. (**E**) Anhedral cassiterite grains highly replaced by sphalerite; the assemblage is cut by a very thin veinlet that hosts some galena. (**F**) Formerly euhedral cassiterite crystals intergrown with pyrite and quartz; both cassiterite and pyrite are partly replaced by sphalerite. (**G**) Arsenopyrite crystals show partial replacement by pyrite and both minerals were extensively replaced by sphalerite; cassiterite occurs as scattered minute relicts. (**H**) Detail of owyheeite, fizélyite and miargyrite that line porosity in sphalerite and cassiterite; miargyrite is locally veined by fizélyite (inset). (**I**) Infilling in porosity within sphalerite, lined with galena, hocartite, diaphorite and pyrargyrite. Key: apy = arsenopyrite; cst = cassiterite; dia = diaphorite; fiz = fizélyite; gn = galena; hoc = hocartite; owy = owyheeite; py = pyrite; pyr = pyrargyrite; qz = quartz; sl = sphalerite.

In the Chorro vein, sphalerite is the main ore mineral (up to 70% modal) and it occurs along appreciable amounts of sulfosalts (Figure 4). Quartz is the only identified gangue mineral; it forms euhedral to anhedral crystals some tens of micrometers long. In general, the vein texture can be described as a mass of sphalerite and sulfosalts that flooded the interstitial space between the crystals of quartz and that contains remnants of earlier minerals (Figure 4A–D). Cassiterite, which is relatively scarce in the Chorro vein, is one of the mineral phases found as anhedral remnants due to its replacement by sphalerite and sulfosalts (Figure 4E,F,H,I). Other phases in a similar textural position are arsenopyrite, which forms subhedral crystals that are up to 200 μm across (Figure 4B), and pyrite, which forms anhedral grains up to 250 μm across (Figure 4C). Massive aggregates of anhedral sphalerite show abundant secondary porosity that is often lined with sulfosalts and galena (Figure 4A,B), and locally replaced by stannite (Figure 4A,E). Garland-like arrays of galena and sulfosalt crystals are locally observed within sphalerite. Sphalerite is, in addition, observed as minute anhedral isolated grains within a mass of sulfosalts in a reactive sequence (Figure 4I,J,L). Minor amounts of galena are lining porosity within pyrite grains (Figure 4G). In the sulfosalt + galena assemblages after sphalerite, galena is found as anhedral corroded and isolated grains with sizes that are up to some tens of micrometers (Figure 4H,I). A wealth of sulfosalts has been identified in samples from the Chorro vein, namely miargyrite, franckeite [$Fe^{2+}(Pb,Sn^{2+})_6Sn^{4+}{}_2Sb_2S_{14}$], boulangerite [$Pb_5Sb_4S_{11}$], teallite [$PbSnS_2$], ramdohrite [$Pb_{5.9}Fe_{0.1}Mn_{0.1}In_{0.1}Cd_{0.2}Ag_{2.8}Sb_{10.8}S_{24}$], diaphorite, hocartite, and fizélyite. Miargyrite occurs as anhedral aggregates that flooded interstitial spaces between subhedral crystals of quartz and corroded grains of pyrite, sphalerite, and cassiterite (Figure 4C). Miargyrite is locally veined by other sulfosalts (i.e ramdohrite and diaphorite; Figure 4K). Franckeite, boulangerite, teallite, and fizélyite mostly form up to 100 μm long needles and bladed crystals (Figure 4F,H,J,L).

The ore mineralogy in the Diez vein is dominated by sulfides, among which sphalerite is the most abundant, with a modal proportion ~75% in the studied samples (Figure 5A–F). The general structure of the vein includes a 2 mm-wide rim that is dominated by anhedral pyrite and subhedral arsenopyrite with sizes that mostly range between 100 and 200 μm, and that are often intergrown with euhedral quartz (Figure 5A,E). Such pyrite belongs to a first stage of mineralization and it is accordingly labelled as pyrite-I. Pyrite-I and arsenopyrite are replaced by sphalerite mostly along irregular replacement fronts; sphalerite is also flooding interstitial spaces between arsenopyrite and pyrite-I and fills corrosion porosity within them (Figure 5A,E). The vein core is almost exclusively composed of massive sphalerite that shows a conspicuous overlying of parallel bands with oscillatory composition that depicts crustiform and drusy patterns that extend inward the vein from the pyrite-I–arsenopyrite–quartz assemblage (Figure 5B,C,F). Close to the contact with the outer pyrite-I–arsenopyrite–quartz "substrate", sphalerite hosts a myriad of micrometer-sized chalcopyrite blebs (chalcopyrite disease texture) that disappear towards the inner bands of sphalerite (Figure 5D). Porosity within massive sphalerite is lined with stannite and, to a lesser extent, with tetrahedrite-group minerals (Figure 5A,E). Stannite also occurs as replacement bands across the bands of sphalerite (Figure 5F). Such an assemblage is cut by 2 mm-thick stringers that are composed of quartz, sulfides and sulfosalts. In general, such veinlets show outer sectors of massive quartz and a central suture of pyrite and sulfosalts (mostly jamesonite [$Pb_4FeSb_6S_{14}$], andorite [$AgPbSb_3S_6$] and boulangerite; Figure 5G). Accordingly, such pyrite within is labelled as pyrite-II. Pyrite-II occurs as anhedral grains that host abundant inclusions of up to 50 μm long needle-like and bladed euhedral jamesonite (Figure 5G–I). Pyrite-II is often wrapped by jamesonite crystals that are partly replaced by an andorite and boulangerite assemblage (Figure 5H). Andorite is rather scarce in such assemblage and it mostly appears as islands that are surrounded by boulangerite, thus suggesting its replacement by the latter (Figure 5I).

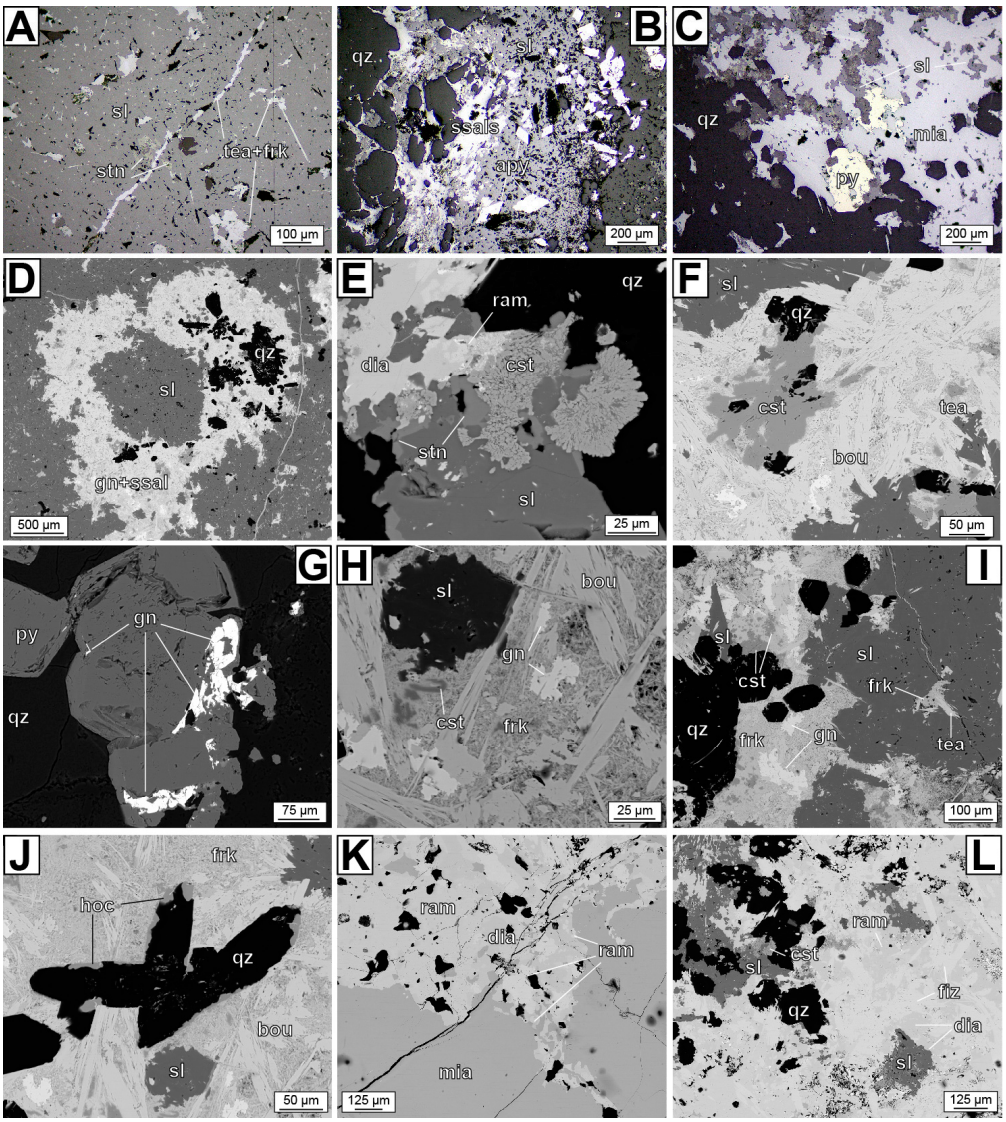

Figure 4. Photomicrographs (reflected light; **A**–**C**) and back-scattered electron images (**D**–**L**) of textural features in the Chorro vein in the Siete Suyos mine. (**A**) Corroded sphalerite with abundant secondary porosity and cut by veinlets lined with teallite and franckeite; sphalerite shows local replacement to stannite. (**B**) Subhedral crystals of arsenopyrite partly replaced by abundant sphalerite, which in turn is partially replaced by an assemblage of fine-grained sulfosalts. (**C**) Corroded pyrite grains and sphalerite extensively replaced by miargyrite. (**D**) Fine-grained quartz, sulfosalts and galena in a garland-like arrangement; the central space and the periphery are flooded by sphalerite. (**E**) Anhedral crystals of cassiterite showing engulfment filled with stannite and sphalerite; in addition, sphalerite is partly replaced and veined by diaphorite and ramdohrite. (**F**) Anhedral cassiterite replaced by boulangerite and teallite. (**G**) Anhedral pyrite with inclusions of galena. (**H**) Relicts of sphalerite and cassiterite in a mass of galena, franckeite and boulangerite; note that galena is partly replaced by the sulfosalts. (**I**) Porosity within and veinlets across sphalerite lined with a fine-grained assemblage of galena, teallite and franckeite; galena, teallite and franckeite also occupy interstitial space between subhedral quartz crystals. (**J**) Subhedral quartz and anhedral sphalerite crystals replaced by hocartite, franckeite and boulangerite. (**K**) Miargyrite veined by fine-grained ramdohrite and diaphorite. (**L**) Anhedral quartz, sphalerite and cassiterite within a mass of diaphorite, fizélyite and ramdohrite. Key: apy = arsenopyrite; bou = boulangerite; cst = cassiterite; dia = diaphorite; frk = franckeite; gn = galena; hoc = hocartite; fiz = fizélyite; mia = miargyrite; py = pyrite; qz = quartz; ram = ramdohrite; sl = sphalerite; ssals = finely intergrown sulfosalts; stn = stannite; tea = teallite.

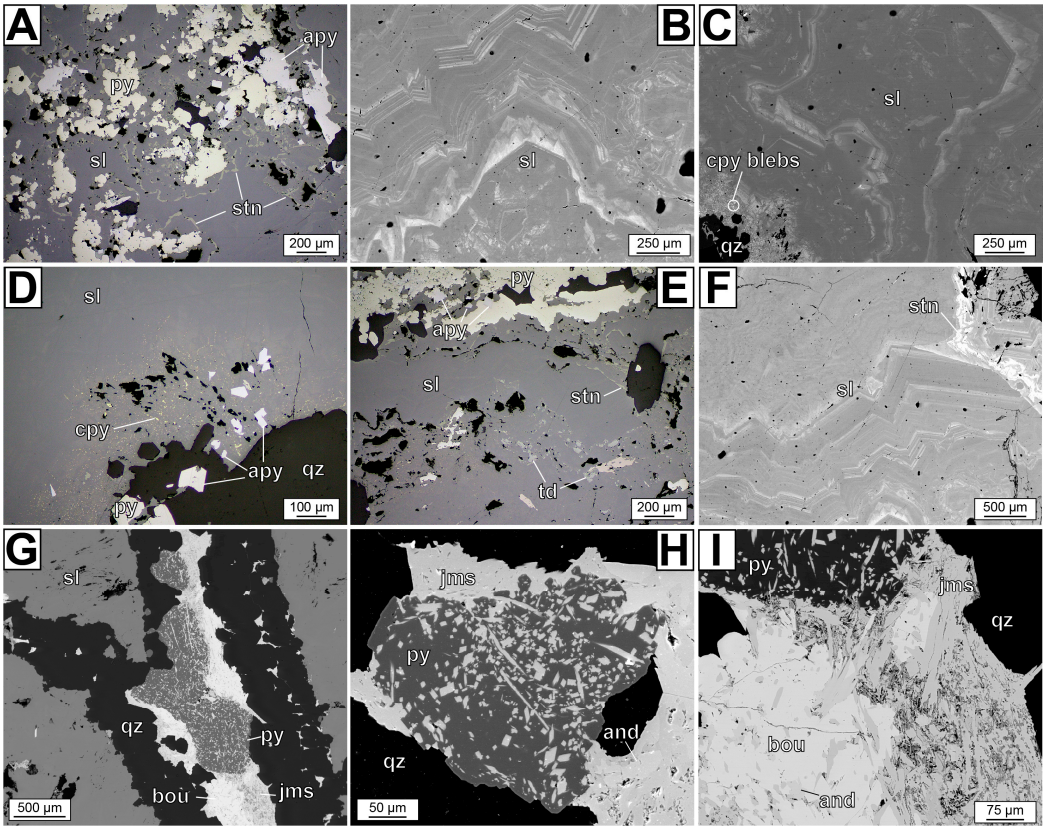

Figure 5. Photomicrographs (reflected light; **A**,**E**,**F**) and back-scattered electron images (**B**,**C**,**F–I**) of textural features in the Diez vein in the Siete Suyos mine. (**A**) Anhedral pyrite and subhedral arsenopyrite grains in a groundmass composed of sphalerite and stannite. (**B**) Conspicuous compositional sub-parallel banding describing crustiform and polygonal patterns in sphalerite; brighter zones correspond to In- and Cu-rich compositions. (**C**) Open-space infilling of alternate bands of In- and Cu-rich (brighter) with Cu- and In-poor (darker) sphalerite; in the bottom left corner, sphalerite in contact with quartz, hosting myriad chalcopyrite blebs. (**D**) Sphalerite in contact with quartz, pyrite and arsenopyrite, with abundant chalcopyrite blebs that fade off outward. (**E**) Pyrite and arsenopyrite giving way to massive sphalerite inward the vein; porosity in sphalerite is mostly lined with stannite and tetrahedrite. (**F**) Parallel bands of sphalerite with contrasting composition in terms of In and Cu, cut by stannite. (**G**) Quartz stringer across sphalerite with a pyrite, jamesonite and boulangerite core. (**H**) Pyrite with micrometer-sized jamesonite inclusions; in the periphery of pyrite crystals, jamesonite is partly replaced by andorite. (**I**) Jamesonite needles and blades replaced by an assemblage of boulangerite and andorite. Key: apy = arsenopyrite; and = andorite; bou = boulangerite; cpy = chalcopyrite; jms = jamesonite; py = pyrite; qz = quartz; sl = sphalerite; stn = stannite; td = tetrahedrite-group minerals.

4.2. Ánimas Mine

The mineralogy and micro-textures of samples from the Ánimas, Burton, Colorada, and Rosario veins in the Ánimas mine are described below.

In the Ánimas vein, the ore mineral assemblage is chiefly composed of pyrite, cassiterite, sphalerite, and stannite-group minerals with significant amounts of sulfosalts, and the main gangue mineral is quartz (Figures 6 and 7). In the outer sectors of the vein, pyrite, cassiterite, and quartz form common interspersed and interlocked crustiform bands, some tens of micrometers thick each (Figure 6A,B). Pyrite within this banded arrangement (pyrite-I) mostly occurs as anhedral crystals with abundant porosity that is lined with micrometer-sized cassiterite crystals and a variety of sulfides and sulfosalts (Figure 6B–D). Pyrite-I is often finely intergrown with variable amounts of marcasite, so that under the petrographic microscope shows slightly whiter sectors with strong pleochroism;

such pyrite–marcasite assemblage is locally recrystallized to "clean" pyrite (pyrite-II) that tends to form euhedral crystals. Cavities in corroded pyrite-I–marcasite crystals are often nicely arranged drawing beehive-like patterns that suggest the pseudomorphic replacement of former crystals with pseudo-hexagonal habit (Figure 6D). Infillings along joints and porosity within pyrite-I often show an outer lining of cassiterite and central stannite (Figure 6D). Cassiterite is more abundant at the shallow levels of the vein (100 and 125 levels) and it is increasingly replaced by stannite-group minerals (Figure 6E,F) at greater depths; stannite-group minerals are indeed much abundant at the 175 and 200 mining levels (Figure 6G), representing up to 50% (modal) of the mineralization in some of the studied samples. Pyrite-I is also either replaced along borders or veined by stannite (Figure 6F,G). Arsenopyrite is up to 5% (modal) in all of the studied samples and it normally forms euhedral crystals up to 300 μm across (long axis) epitaxial to pyrite-I (± marcasite, Figure 6H) or intergrown and included within pyrite-I and quartz (Figure 6I–K). In Figure 6J, a euhedral crystal of a monazite-group mineral and arsenopyrite within pyrite-I impinge upon one another. Sphalerite is found in all the studied samples (up to 20% modal) and it mostly concentrates along the central domains of the vein and subsidiary veinlets. It is commonly observed interstitial to quartz, pyrite and cassiterite (Figure 6I) or replacing (along irregular fronts or veinlets) pyrite-I (Figure 6I,L). Sphalerite and stannite-group minerals form intricate intergrowths and mutual veining that suggest that, at least in part, these two sulfides coevally crystallized (Figure 7A). Galena is rather scanty in the studied samples and systematically appears as minute anhedral crystals lining porosity within corroded crystals of the sulfides mentioned above and cassiterite. In addition, galena is observed as an infilling of stringers and cracks that cut the sulfosalt assemblage above.

Samples from the Ánimas vein host a wealth of sulfosalts, which mostly occur lining porosity and filling interstitial space between pyrite, cassiterite, arsenopyrite, and quartz. Jamesonite occurs as minute needles of less than 5 μm in diameter and some tens of micrometers in length, or as subparallel 200 μm long bladed crystals that form columnar masses (Figure 7A–E,G). Jamesonite is replaced along rims and twining planes on {100} by other sulfosalts and also by sphalerite and stannite (Figure 7E–G). Tetrahedrite-group minerals (tetrahedrite and freibergite; see below) form anhedral aggregates that adapt to the morphology of the available space or form irregular replacement fronts on stannite, sphalerite, and jamesonite (Figure 7A,B,E,H). Andorite and miargyrite show common mutual boundaries and fine intergrowths (Figure 7D,G), some of which recall myrmekitic textures (Figure 7F). Minute miargyrite crystals are observed along the contacts between tetrahedrite-group minerals and pyrite (Figure 7H). Pyrargyrite is rare in the Ánimas vein and it mostly occurs along contacts between andorite and miargyrite or replacing them (Figure 7G). Local fizélyite occupies interstitial space between boulangerite subhedral crystals (Figure 7I). Minor amounts of staročeskéite [$Ag_{0.70}Pb_{1.60}(Bi_{1.35}Sb_{1.35})_{\Sigma 2.70}S_6$] are observed lining porosity in cassiterite along with stannite and other sulfosalts; when found along with stannite, staročeskéite concentrates along the rims of the porosity or veins stannite, thus pointing to a later crystallization. Traces of other sulfosalts, such as franckeite, oscarkempffite [$Ag_{10}Pb_4(Sb_{17}Bi_9)S_{48}$], ramdohrite, semseyite [$Pb_9Sb_8S_{21}$], and terrywallaceite [$AgPb(Sb,Bi)_3S_6$] have also been identified in the Ánimas vein.

The studied sample from the Burton vein (Figure 8) is mostly composed of pyrite (~75% modal). Pyrite occurs as highly corroded anhedral grains with abundant porosity often arranged describing orbicular, crustiform and polygonal patterns (Figure 8A–E). Scattered euhedral quartz crystals between 100 μm and 1 mm in length show mutual straight boundaries with pyrite (Figure 8C). Remnants of arsenopyrite crystals up to 300 μm across are encapsulated by pyrite (Figure 8A,E,F). Cassiterite, which is a trace mineral in the sample, occurs as anhedral grains up to 150 μm in diameter that show pervasive engulfment and porosity due to replacement by later sulfides and sulfosalts (Figure 8G). The conspicuous porosity within and the corrosion gulfs around pyrite are mostly lined with stannite, which is relatively abundant (~20% modal; Figure 8A–E); stannite is also common as interstitial space infillings between pyrite and quartz (Figure 8C). In similar textural positions as stannite occur tetrahedrite-group minerals and chalcopyrite (Figure 8A,B,D–G). Stannite and tetrahedrite-group minerals show complex intergrowths in which the first is apparently veined and replaced along very irregular fronts by the second. Tetrahedrite-group minerals host micrometer-

sized inclusions of chalcopyrite (Figure 8B) and both minerals form complex intergrowths in which chalcopyrite veins tetrahedrite-group minerals, thus suggesting a later crystallization of the former (Figure 8E,F). Porosity in pyrite is also filled with trace amounts of galena, oscarkempffite, and miargyrite, which partially replaced stannite (Figure 8H,I).

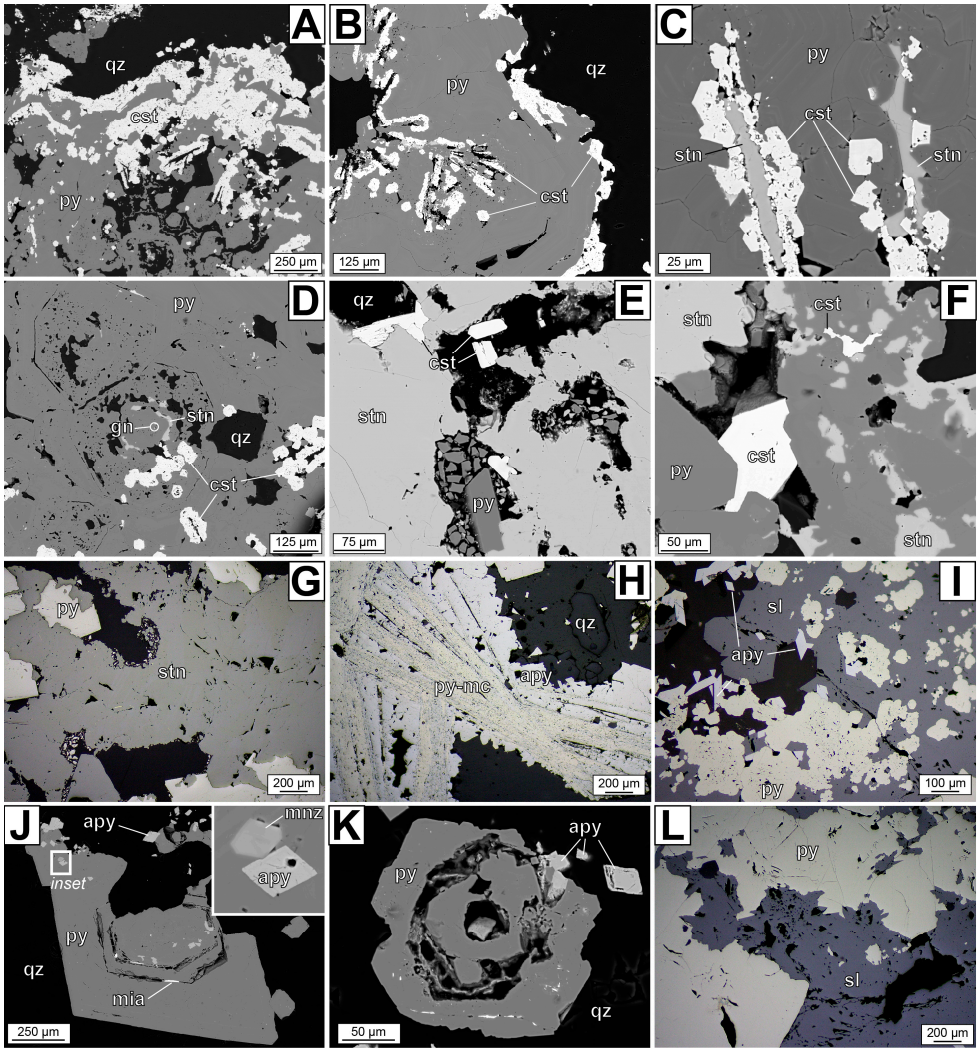

Figure 6. Back-scattered electron images (**A**–**D**,**F**,**J**,**K**) and photomicrographs (reflected light; **E**,**G**–**I**,**L**) of textural features in the Ánimas vein in the Ánimas mine. (**A**) Interspersed microbands of pyrite and cassiterite; in addition, cassiterite lines porosity in pyrite, which shows beehive-like replacement textures. (**B**) Detail of cassiterite mineralization along cracks, cavities and rims of pyrite. (**C**) Vugs in pyrite are lined with cassiterite and a central infill of stannite. (**D**) Cavities in pyrite denote hexagonal structures and draw beehive-like textures; cavities are filled with cassiterite, stannite and traces of galena. (**E**) Detail of subhedral cassiterite crystals replaced by stannite, which also replaced pyrite. (**F**) Cassiterite relicts after pervasive replacement by stannite. (**G**) Pervasive replacement of pyrite crystals by stannite. (**H**) Detail of intergrown pyrite–marcasite pseudomorphic after pyrrhotite tabular crystals, which are epitaxially overgrown by subhedral crystals of arsenopyrite. (**I**) Sphalerite replacement of an assemblage of euhedral arsenopyrite and subhedral and anhedral pyrite crystals. (**J**) Corroded pyrite crystal with inclusions of arsenopyrite and monazite, and cavities lined with miargyrite. (**K**) Arsenopyrite intergrown with pyrite, the latter showing a pseudo-hexagonal morphology. (**L**) Pervasive replacement of anhedral pyrite grains by sphalerite; both minerals show abundant cavities that denote corrosion. Key: apy = arsenopyrite; cst = cassiterite; gn = galena; mc = marcasite; mia = miargyrite; mnz = monazite-group minerals; py = pyrite; qz = quartz; sl = sphalerite; stn = stannite.

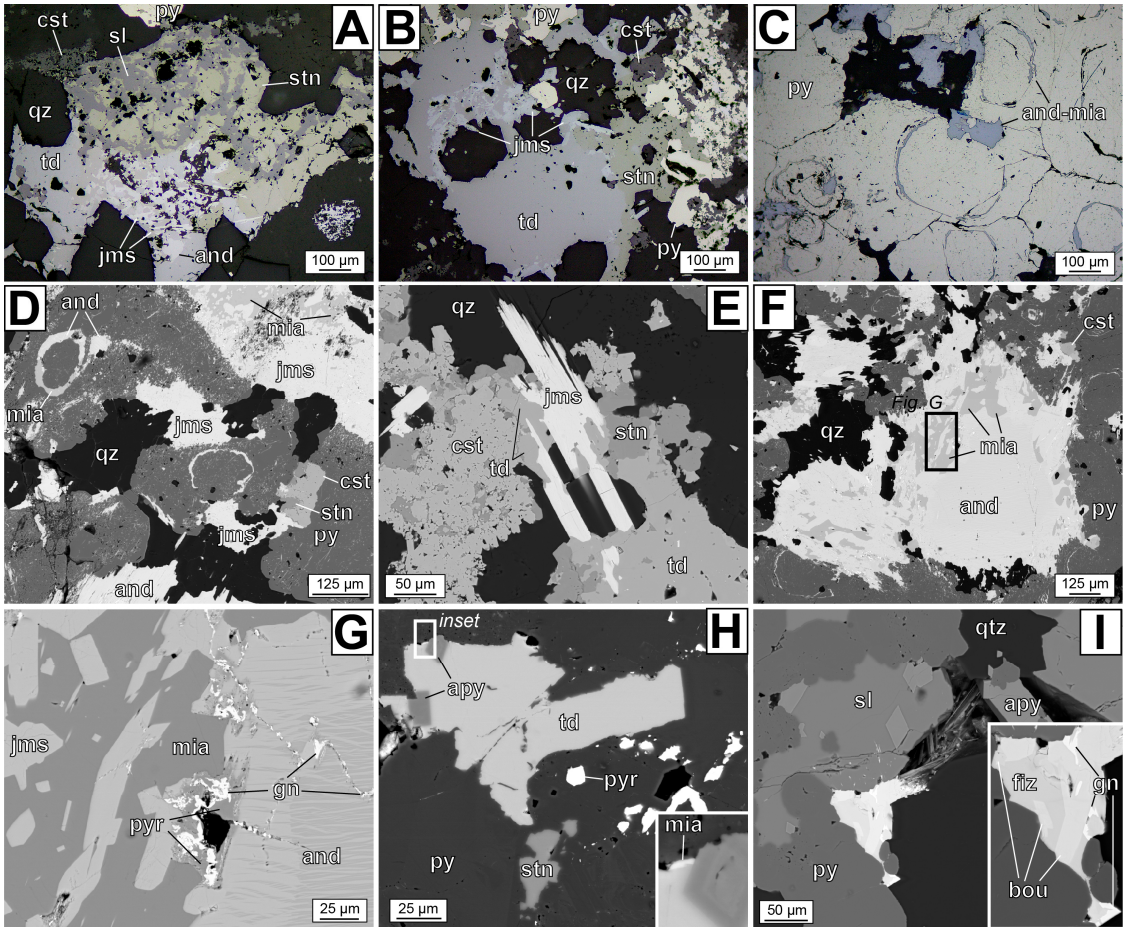

Figure 7. Photomicrographs (reflected light; **A**–**C**) and back-scattered electron images (**D**–**I**) of textural features of sulfosalts in the Ánimas vein in the Ánimas mine. (**A**) Interstitial space between euhedral quartz crystals filled with an assemblage of sulfides and sulfosalts; early sphalerite is veined by stannite, which in turn is veined and cut by anhedral crystals of tetrahedrite-group minerals, andorite and euhedral jamesonite. (**B**) Relicts of pyrite and cassiterite replaced by an assemblage of stannite, tetrahedrite-group minerals and jamesonite. (**C**) Beehive-like pyrite (pseudomorphic replacement of pseudo-hexagonal crystals) showing abundant porosity, lined with sulfosalts (mostly andorite and miargyrite). (**D**) Corroded pyrite crystals, with porosity lined with andorite, miargyrite, and stannite; in addition, an assemblage of jamesonite, miargyrite and andorite replaced pyrite from its borders inwards. Note the replacement of cassiterite by stannite in the bottom left corner or the image. (**E**) Bladed crystals of jamesonite and subhedral crystals of cassiterite replaced by stannite and tetrahedrite-group minerals; note also tetrahedrite-group minerals veining stannite. (**F**) Interstitial space between pyrite and quartz crystals lined with andorite and miargyrite. (**G**) Minute inclusions of galena concentrate along cracks, contacts and voids in an assemblage of miargyrite, pyrargyrite and jamesonite; note pyrargyrite replacing andorite and miargyrite. The location of this image is shown in **F**. (**H**) Interstitial space between pyrite and epitaxial arsenopyrite lined with tetrahedrite-group minerals and stannite; miargyrite is observed along the contact between pyrite and tetrahedrite-group minerals (inset). (**I**) Interstitial space between sulfides and quartz lined with boulangerite, fizélyite and galena; galena concentrates along the rims of the cavity and cracks in the fizélyite and boulangerite assemblage. Key: and = andorite; apy = arsenopyrite; bou = boulangerite; cst = cassiterite; fiz = fizélyite; gn = galena; jms = jamesonite; mia = miargyrite; py = pyrite; pyr = pyrargyrite; qz = quartz; sl = sphalerite; stn = stannite; td = tetrahedrite group.

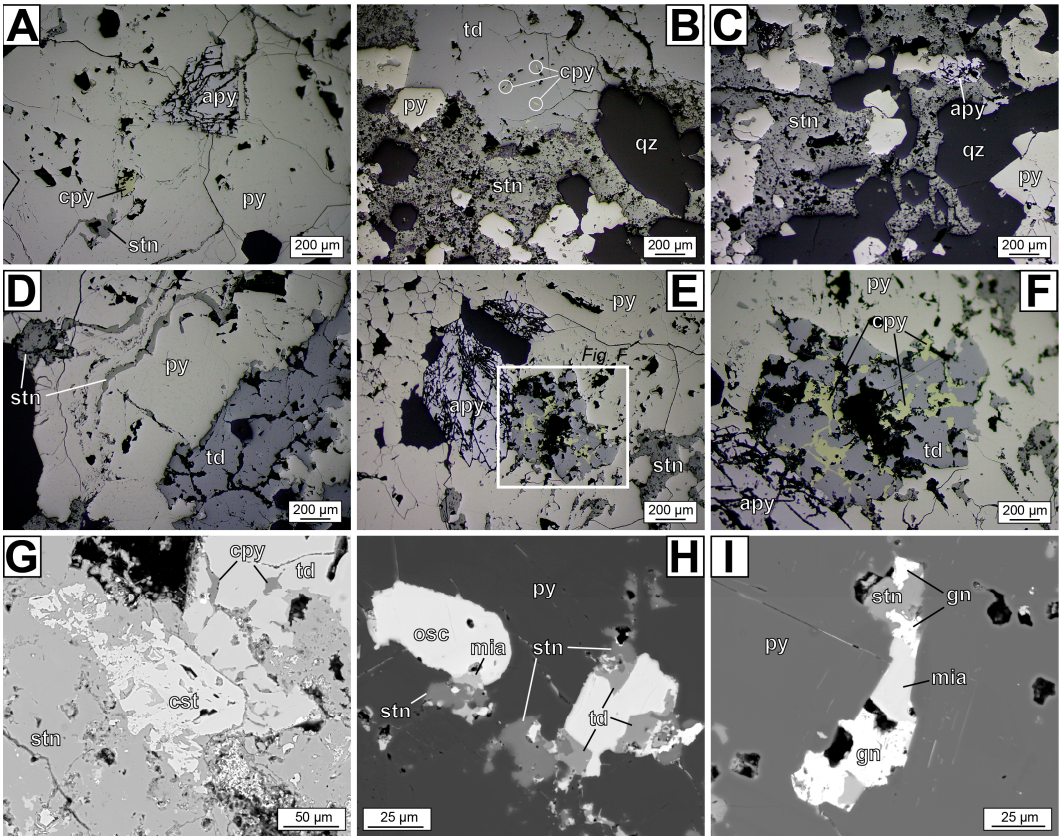

Figure 8. Photomicrographs (reflected light; **A**–**F**) and back-scattered electron images (**G**–**I**) of textural features in the Burton vein in the Ánimas mine. (**A**) Corroded pyrite and arsenopyrite, with porosity lined with stannite and chalcopyrite. (**B**) Stannite and tetrahedrite-group minerals filling interstitial space between euhedral crystals of quartz and corroded pyrite; tetrahedrite-group minerals host micrometer-sized inclusions of chalcopyrite. (**C**) Stannite occupying interstitial space among quartz, pyrite and arsenopyrite crystals. (**D**) Crustiform pyrite aggregates with conspicuous porosity and corrosion engulfment, lined with stannite and tetrahedrite-group minerals. (**E**) Stannite, tetrahedrite and chalcopyrite lining secondary porosity in pyrite and arsenopyrite. (**F**) Detail of tetrahedrite-group minerals and chalcopyrite infilling (location in **E**); note that chalcopyrite veins tetrahedrite-group minerals. (**G**) Tetrahedrite-group minerals with inclusions of chalcopyrite and a relict of a cassiterite grain replaced by stannite. (**H**) Detail of stannite, tetrahedrite-group minerals, miargyrite and oscarkempffite infillings in pyrite cavities. (**I**) Detail of a stannite, miargyrite and galena infilling in pyrite cavities; note that galena veins stannite. Key: apy = arsenopyrite; cpy = chalcopyrite; cst = cassiterite; gn = galena; mia = miargyrite; osc = oscarkempffite; py = pyrite; qz = quartz; stn = stannite; td = tetrahedrite-group.

The Colorada vein shows marked internal banding that is defined by lineal arrangements of ore minerals separated by bands of quartz (Figure 9A). The main ore phases are cassiterite, arsenopyrite, and tetrahedrite-group minerals, which represent >90% modal altogether of the ore. Cassiterite forms anhedral grains, less than 150 µm in size, mostly intergrown with quartz and, to a lesser extent, with pyrite and arsenopyrite in the rims of the vein. Pyrite forms anhedral grains both as masses or isolated, and has been pervasively replaced by arsenopyrite and other sulfides and sulfosalts (Figure 9A–C). Cassiterite and the pyrite–arsenopyrite assemblage are extensively replaced by stannite and tetrahedrite-group minerals, which also flooded the interstitial space between these minerals (Figure 9B–D,G–J). Local wolframite (including both ferberite and hübnerite compositions) appears as subhedral and euhedral tabular and short prismatic crystals up to 150 µm in length that often form parallel aggregates within quartz (Figure 9F); minute inclusions of wolframite are also observed within porosity in pyrite (Figure 9K). The concentration of stannite and, particularly, of tetrahedrite-

group minerals increases towards the vein core, even forming almost monomineralic massive aggregates. Stannite is commonly found isolated within or veined by tetrahedrite-group minerals (Figure 9D), thus indicating a later crystallization of the latter. Chalcopyrite is rare in the Colorada vein and it occurs as scattered inclusions (some tens of μm in diameter) within tetrahedrite-group minerals (Figure 9D). Chalcopyrite is also observed lining porosity within other phase minerals such as quartz and pyrite, and it is locally veined by a second generation of stannite (Figure 9E). Cassiterite and sulfides form garland-like aggregates that draw hexagonal shapes (Figure 9J), in which the central part is occupied by quartz. Porosity and interstitial space among quartz, cassiterite, and the above described sulfides and sulfosalts in the Colorada vein are often lined with oscarkempffite, aramayoite (Figure 9G,J), miargyrite, and terrywallaceite. Pyrite and cassiterite show local replacement by a mineral with the same composition as angelellite [$Fe^{3+}_4(AsO_4)_2O_3$] in the form of colloform aggregates (Figure 9K,L). Secondary porosity in pyrite draws pseudo-hexagonal patterns, whereas, in cassiterite, the porosity is mostly irregular.

The Rosario vein is mostly composed of pyrite, marcasite, and stannite group minerals, and quartz is the main gangue mineral. Fine-grained marcasite and pyrite (pyrite-I) form slabs of some hundreds of micrometers in length that tend to group into radial aggregates (Figure 10A,B). Aggregates of tabular pyrite and marcasite show myriads of micrometer-sized cavities that distribute in trails parallel to the long axis of the slabs. The fine intergrowths of pyrite–marcasite are in part recrystallized to subhedral and anhedral equant pyrite grains (pyrite-II), between 100 and 300 μm in diameter and a low porosity that results in a more homogeneous aspect when compared to marcasite–pyrite-I aggregates (Figure 10A,B). The pyrite-II grains are not completely homogeneous in color and combine zones with a cream color and an isotropic optical behavior with zones of a clearer (almost white) color and a fair pleochroism that might indicate an incomplete recrystallization of marcasite to pyrite (subtle but visible in Figure 10C). Pyrite (both generations) and marcasite constitute the "skeleton" of the outer sectors of the vein, and the rest of the minerals appear as their replacements or interstitial to them. Cassiterite, which is scarce in the Rosario vein, occurs as micrometer-sized anhedral crystals that form aggregates up to 1 mm across and are locally intergrown with pyrite crystals (Figure 10C). Sphalerite is also scarce and it is only observed as anhedral grains completely surrounded by quartz groundmasses. Pyrite, marcasite and cassiterite are partly replaced by stannite-group minerals along irregular replacement fronts (Figure 10A–C,G). Stannite-group minerals are also common as infillings of porosity within pyrite(±marcasite) and highlight orbicular to polygonal patterns in the distribution of the porosity cavities (Figure 10D,E). The vein grades inwards to a chalcopyrite- and stannite-group minerals-rich assemblage in stark contrast with the abundance of pyrite–marcasite in the vein rims. In the core of the Rosario vein, stannite-group minerals form a massive aggregate that includes famatinite [Cu_3SbS_4] and stannite. Famatinite is much scarcer than stannite and it occurs as islands that are surrounded and veined by stannite, thus suggesting its earlier formation. Chalcopyrite is found in the form of inclusions within stannite and famatinite and forming thin stringers across them; chalcopyrite might also accumulate along the contacts between pyrite and the massive infilling of stannite-group minerals (Figure 10F). Teallite is particularly abundant in the studied samples of the Rosario vein and it forms subhedral platy crystals that are up to 150 μm in length. Teallite, along with traces of terrywallaceite, occurs lining porosity within pyrite-marcasite, quartz and cassiterite (Figure 10C,H,I). In the same textural position occurs bismuthinite, which is observed to replace and vein terrywallaceite and to host some minute inclusions of native bismuth (Figure 10I).

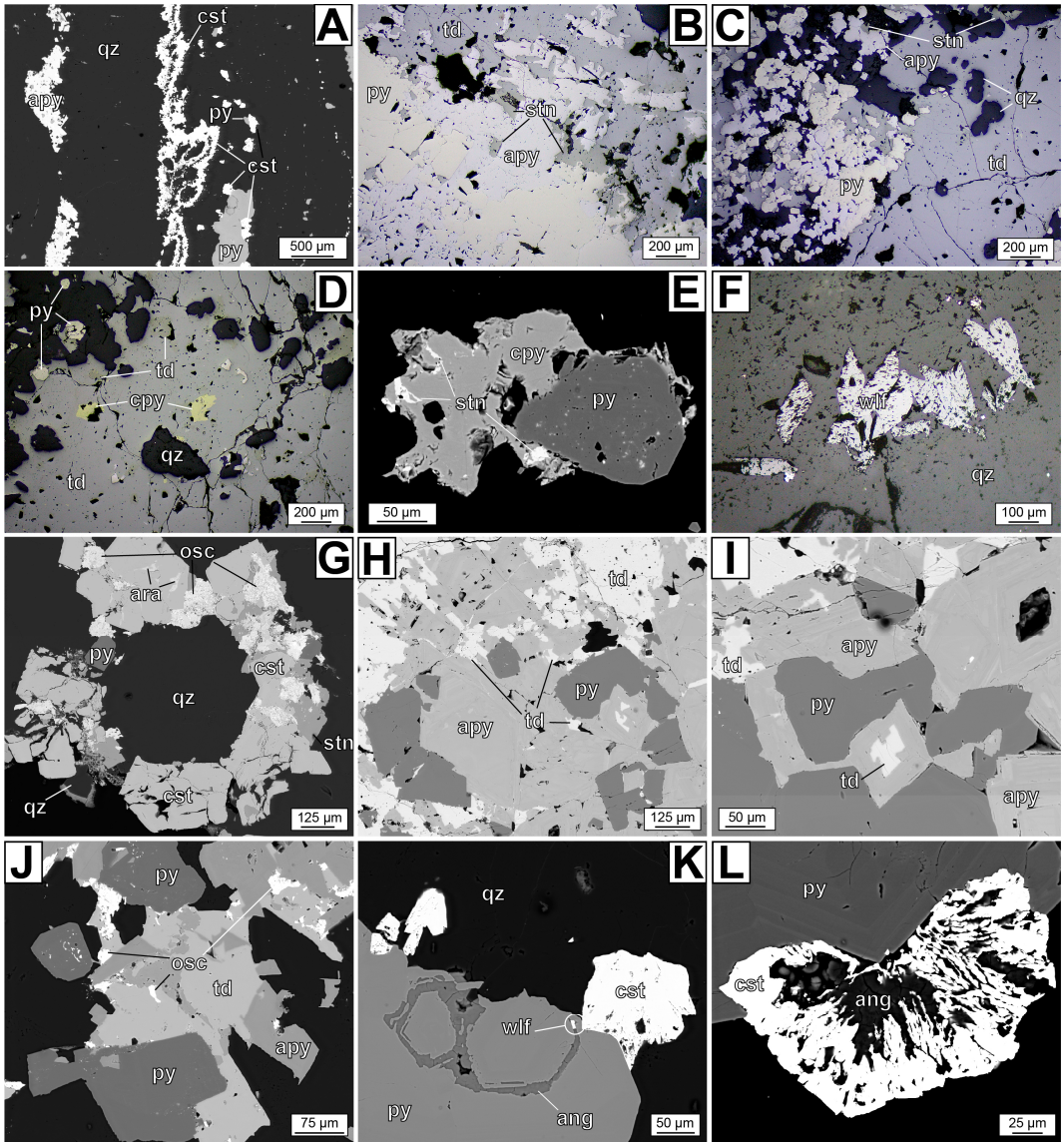

Figure 9. Back-scattered electron images (**A**,**G**–**L**) and photomicrographs (reflected light; **B**–**F**) of textural features in the Colorada vein in the Ánimas mine. (**A**) Parallel bands of quartz, cassiterite and sulfides (mostly arsenopyrite and pyrite). (**B**) Anhedral crystals of pyrite replaced by arsenopyrite, in turn replaced by stannite and tetrahedrite-group minerals. (**C**) Interstitial space between corroded crystals of pyrite and arsenopyrite lined with stannite and tetrahedrite-group minerals. (**D**) Inclusions of chalcopyrite in a mass of stannite and tetrahedrite-group minerals. (**E**) Detail of a chalcopyrite-stannite inclusion within quartz along with an anhedral crystal of pyrite; note stannite stringers across chalcopyrite. (**F**) Micrometer-scale euhedral wolframite crystals in a quartz groundmass. (**G**) Cassiterite-stannite-pyrite garland; note cassiterite crystals replaced by stannite, both of them hosting abundant oscarkempffite and staročeskéite inclusions. (H) Anhedral pyrite crystals conspicuously replaced by arsenopyrite, in turn intensely replaced and veined by tetrahedrite-group minerals. (**I**) Detail of tetrahedrite-group minerals replacing arsenopyrite; note the marked zoning of arsenopyrite. (**J**) Abundant oscarkempffite lining cavities in pyrite, arsenopyrite and tetrahedrite-group minerals. (**K**) Cassiterite and pyrite intergrowths; note a minute wolframite crystal in porosity, which is mostly filled with angelellite. (**L**) Detail of an intergrowth between pyrite and cassiterite; cassiterite is anhedral and shows cavities lined with angelellite. Key: ang = angelellite; apy = arsenopyrite; ara = aramayoite; cpy = chalcopyrite; cst = cassiterite; osc = oscarkempffite; py = pyrite; qz = quartz; stn = stannite; td = tetrahedrite-group; wlf = wolframite.

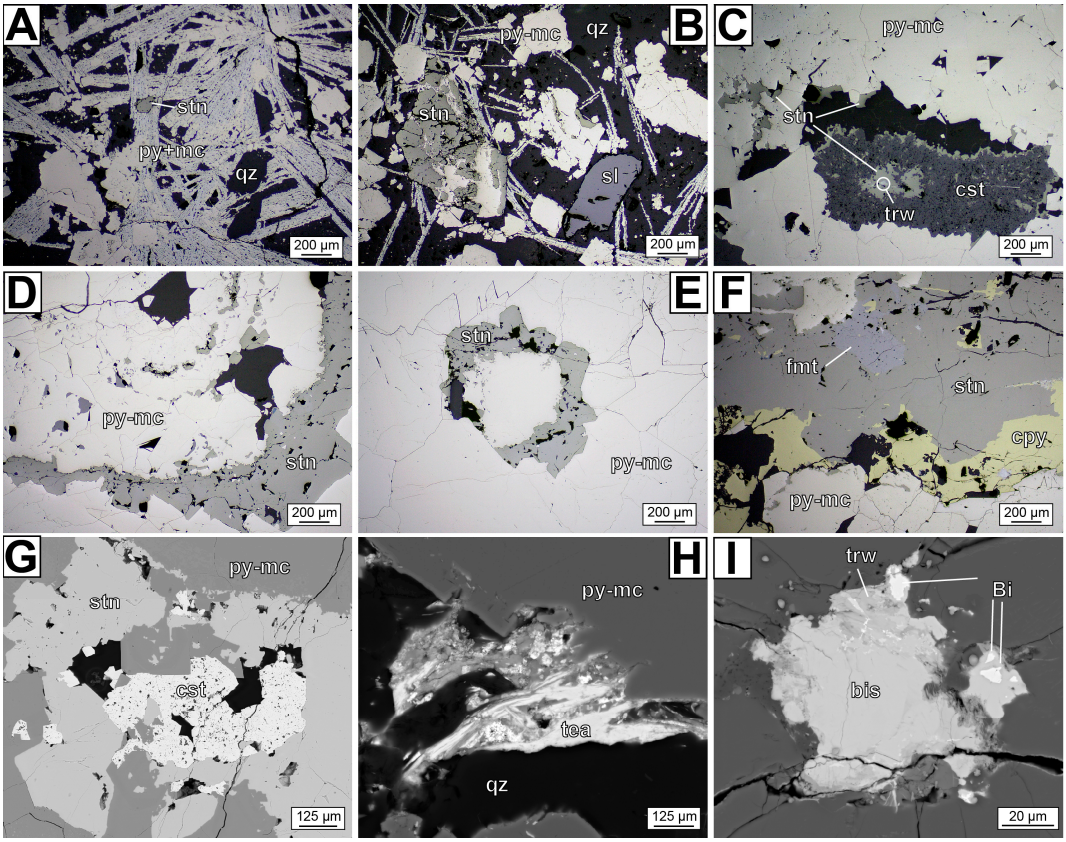

Figure 10. Photomicrographs (reflected light; **A–F**) and back-scattered electron images (**G–I**) of textural features in the Rosario vein in the Ánimas mine. (**A**) Radial aggregates of tabular twined marcasite crystals (white) after tabular pyrrhotite partly recrystallized to pyrite (creamy) and stannite. (**B**) Pyrite-marcasite aggregate partly replaced by stannite; isolated grains of sphalerite are occluded in quartz. (**C**) Aggregate of anhedral cassiterite crystals intergrown with pyrite-marcasite; porosity in both minerals lined with stannite. (**D**) Detail of stannite infilling in concentrically-arranged porosity in pyrite. (**E**) Porosity in pyrite, which is partly lined with stannite, drawing a pseudo-hexagonal pattern. (**F**) Chalcopyrite veining stannite group minerals with famatinite in the vein core; famatinite is partly replaced by stannite. (**G**) Cassiterite and pyrite pervasively replaced by stannite along irregular replacement fronts. (**H**) Teallite platy crystals in the contact between pyrite and quartz. (**I**) Cavity in pyrite lined with stannite, terrywallaceite and native bismuth. Key: apy = arsenopyrite; Bi = native bismuth; bis = bismuthinite; cpy = chalcopyrite; cst = cassiterite; fmt = famatinite; mc = marcasite; py = pyrite; qz = quartz; sl = sphalerite; stn = stannite; tea = teallite; trw = terrywallaceite.

4.3. Chocaya Mine

When compared to veins in the Ánimas and Siete Suyos mines, the mineralogy in the Nueva vein in the Chocaya mine is relatively simple, as it consists in base-metal sulfides nearly in its entirety (Figure 11). Sphalerite and marcasite-pyrite intergrowths constitute the 80% (modal) of ore assemblages. Marcasite–pyrite are commonly concentrated towards the rims of the main vein and associated secondary veinlets, close or along the contacts with wall rocks, whereas sphalerite normally occupies the vein cores. The marcasite–pyrite assemblage forms masses of corroded anhedral grains with abundant porosity lined with other sulfides and quartz (Figure 11A–I,L). Grayish white growth zones (somewhat darker than marcasite) with a strong anisotropy in the iron sulfide aggregates might correspond to relicts of an intermediate product after pyrrhotite (see [75,76]). Pyrrhotite relicts between a few μm and some hundreds μm across are commonly observed within the masses of marcasite–pyrite (– intermediate product; Figure 11B,C,K) and suggest that marcasite–pyrite are products of its replacement. The recrystallization of pyrrhotite to form fine-grained marcasite-pyrite(-intermediate product) is further supported by the almost pseudomorphic replacement that resulted in hexagonal patterns (Figure 11J). These probably represent (001) faces of a hexagonal mineral. Porosity in the marcasite–pyrite masses is often oriented along the {100} planes of allegedly replaced pyrrhotite. Detailed observations reveal that pyrrhotite inclusions within marcasite–pyrite (– intermediate product) are often aligned with porosity (Figure 11K). Fine-grained marcasite is partly recrystallized to subhedral pyrite (Figure 11H,I) and therefore a second generation of pyrite (pyrite-II) is considered. Arsenopyrite occurs in minor amounts in the Nueva vein. It forms euhedral and subhedral crystals some tens of micrometers across, which are mostly decorating the contacts between iron sulfide- and sphalerite-rich bands (Figure 11E,F). Sphalerite and galena generally occur as anhedral grains interstitial to pyrrhotite–marcasite–pyrite and arsenopyrite, lining porosity in corroded iron sulfides and forming bands or masses that filled the central portions of the vein and veinlets. Figure 11H shows a veinlet of sphalerite and galena that cuts a mass of marcasite-pyrite; galena concentrates mostly along the rims of this veinlet. It is common that galena and traces of stannite line cavities in sphalerite (Figure 11C), thus suggesting their late crystallization. Bands of sphalerite with contrasting compositions are arranged parallel to the vein banding. Traces of argyrodite [Ag_8GeS_6] and acanthite form very fine intergrowths that replace galena and that lined interstices between galena and sphalerite.

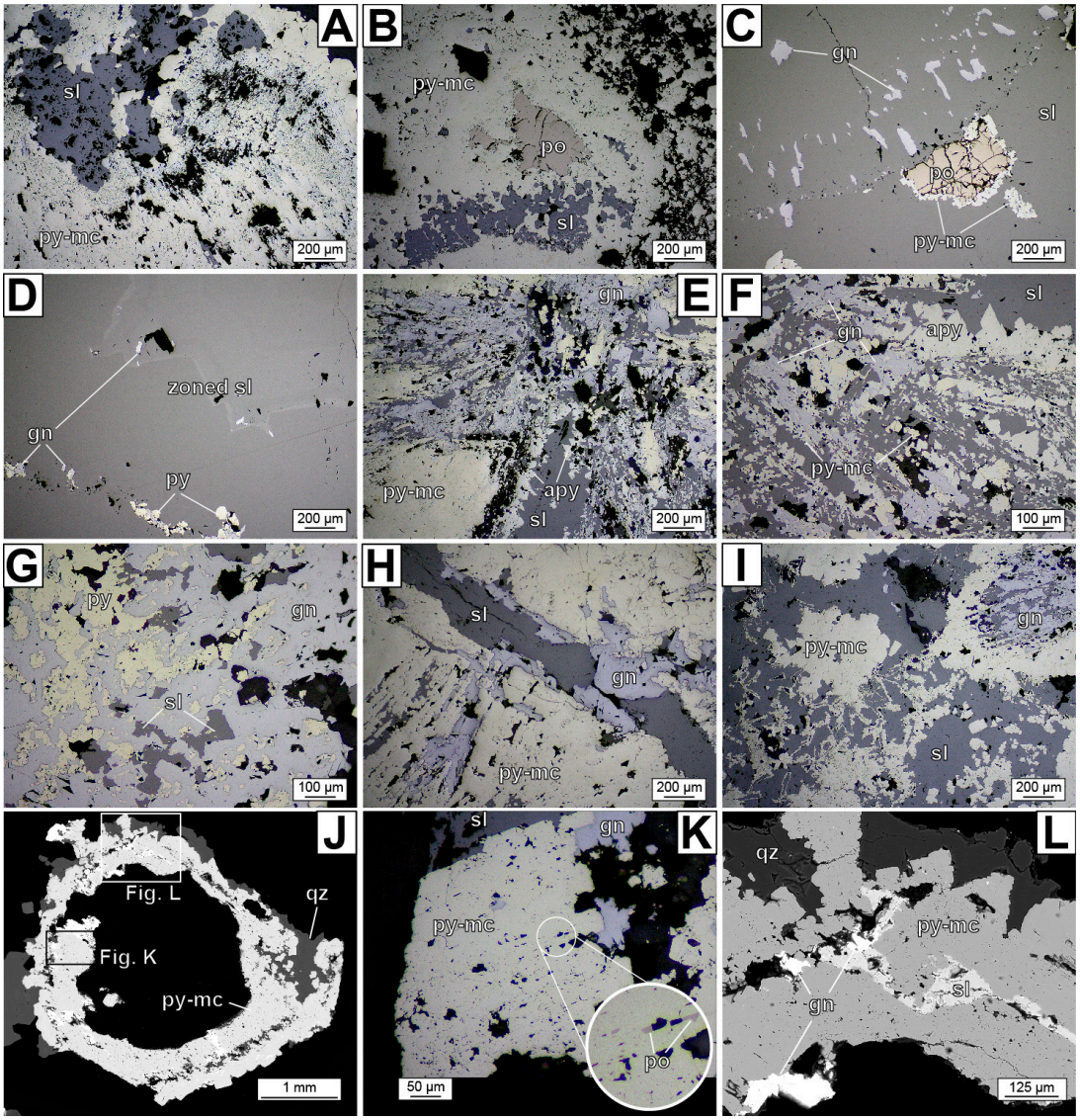

Figure 11. Photomicrographs (reflected light; **A**–**I**,**K**) and back-scattered electron images (**J**,**L**) of textural features in the Nueva vein in the Chocaya mine. (**A**) Fine- and medium-grained marcasite replacing pyrrhotite, partly recrystallized to pyrite. (**B**) Pyrrhotite relict replaced by a marcasite-pyrite and sphalerite assemblage. (**C**) Massive sphalerite hosting a pyrrhotite relict that is partly replaced by marcasite-pyrite; porosity in corroded sphalerite is lined with galena. (**D**) Bands of sphalerite with contrasting chemical composition; the porosity is lined with pyrite and galena. (**E**) Corroded grains of pyrite-marcasite aggregates (pseudomorphs after pyrrhotite) showing oriented porosity lined with sphalerite-galena and cut by an arsenopyrite-sphalerite-galena veinlet (center-bottom of the image; note that arsenopyrite is mostly distributed along the vein rims, and sphalerite concentrates towards its core). (**F**) Complex replacement of the assemblage marcasite–pyrite by arsenopyrite, sphalerite and galena. (**G**) Reactive replacement sequence including early pyrite replaced by sphalerite, which in turn is replaced by galena. (**H**) Sphalerite–galena stringer cutting a marcasite mass (almost completely recrystallized to pyrite); note that galena concentrates along the stringer rim; oriented porosity in corroded marcasite-pyrite (following the cleavages of the former pyrrhotite) is lined with sphalerite and galena. (**I**) Pervasive replacement of marcasite (mostly recrystallized to pyrite) by sphalerite and galena. (**J**) Pseudomorphic replacement of marcasite-pyrite and minor amounts of other sulfides of a pseudohexagonal crystal of pyrrhotite. (**K**) Pyrite–marcasite assemblage with oriented pyrrhotite inclusions (inset; location in **J**). (**L**) Detail of a marcasite-pyrite pseudomorph after pyrrhotite infiltrated by sphalerite and galena (location in **J**). Key: apy = arsenopyrite; gn = galena; mc = marcasite; po = pyrrhotite; py = pyrite; qz = quartz; sl = sphalerite; stn = stannite.

5. Ore Mineral Geochemistry

5.1. In-Bearing Minerals

Relevant indium contents were found in sphalerite (up to 9.66 wt.% In), wurtzite (up to 1.61 wt.% In), stannite-group minerals (up to 4.11 wt.% In), cassiterite (up to 0.25 wt.% In_2O_3), and ramdohrite (up to 0.24 wt.% In).

Sphalerite shows a relatively wide compositional spectrum in Fe, Cu, In and Cd. Table 1 shows a summary of the compositions of the studied sphalerite grains. Although Fe contents in sphalerite peak at the Ánimas mine, similarly wide compositional ranges were found in the three studied mines: between 7.4 and 27.7 mol. % FeS in the Ánimas mine, between 0.0 and 28.8 mol. % FeS in the Chocaya mine, and between 2.3 and 19.6 mol. % FeS in the Siete Suyos mine (Figure 12A). Despite its variations, the average Cu contents in sphalerite are higher in the Siete Suyos (average = 0.85 wt.%) than in Ánimas (average = 0.62 wt.%) and Chocaya (average = 0.12 wt.%) mines (Figure 12B). The concentration of Cu is particularly high in sphalerite from the Diez vein (up to 5.81 wt.%; average = 1.19 wt.%). The Sn contents in sphalerite (up to 4.90 wt.%) are very erratic in the three mines. Similar to Cu, In contents in sphalerite tend to peak in the Siete Suyos mine (up to 9.76 wt.%, average = 0.83 wt.%) and are lower in the Ánimas (up to 2.37 wt.%, average = 0.21 wt.%) and the Chocaya (up to 1.82 wt.%, average = 0.14 wt.%; Figure 12C) mines. Indium contents in sphalerite are particularly high in the Diez vein (up to 8.62 wt.%). Indium contents in sphalerite increase with depth: in the Siete Suyos mine, the average content in the Chorro vein at the 14 level is of 0.35 wt.% In (up to 0.97 wt.% In), and at the 16 level is 1.10 wt.% (up to 2.47 wt.% In; Figure 12D). In the Arturo vein, the average contents are 0.05 wt.% In at the 19 level, 0.08 wt.% In at the 20 level, and 0.22 wt.% In at the 21 level. This trend is also observed in sphalerite from the Ánimas vein in the eponymous mine, in which the average concentration is 0.20 wt.% In at the 125 level and 0.45 wt.% In at the 175 level, although the maximum values (up to 2.37 wt.%, being identified as an outlier value, and 0.94 wt.%, respectively) obscure such a trend (Figure 12D). The contents in other critical metals, such as Ge, in sphalerite from the three mines are systematically very low, being mostly below their detection limits. The maximum Cd contents in sphalerite are 1.41 wt.% Cd in the Siete Suyos mine, 1.04 wt.% Cd in the Ánimas mine, and 2.82 wt.% Cd in the Chocaya mine, although the average values are around ~0.5 wt.% Cd in the three mines.

The measured atomic proportions of Zn and Fe in sphalerite yield a negative correlation and, in the Zn vs. Fe (a.p.f.u.) binary diagram in Figure 13, most compositions lie along the Zn + Fe = 1 (a.p.f.u.) line, thus indicating a dominant substitution between both elements. Nevertheless, a significant number of analyses plot below this line, thus pointing to a deficient occupancy of the cationic position in terms of Zn and Fe alone. In the Fe + Cu + Sn + Cd + In vs. Zn diagram in Figure 13 virtually the entire analyses plot along the Fe + Cu + Sn + Cd + In + Zn = 1 line, which suggests that, besides Fe, coupled substitutions involving other cations also operated (e.g., Zn ↔ Fe + Cu + Sn). Indium contents do not show a clear correlation neither with Fe nor with Zn (Figure 13). The In vs. Zn diagram in Figure 13 shows a broad dispersion of data, with enrichment in In below the Zn + In = 1 line and mostly grouped along and below the sphalerite-roquesite tie-line. Although the enrichment in In generally occurs in Fe-rich sphalerite (mostly between 0.05 and 0.20 a.p.f.u.), a trend towards In enrichment in Fe-poor sphalerite occurs in the Chocaya mine (Figure 13). The atomic concentrations of In and Cu yield a positive correlation, so that, in Figure 13, most of the analyses plot along the Cu/In = 1 line, thus suggesting a coupled substitution of Zn by Cu + In. In contrast, Sn and In do not correlate at all. The positive correlation between In and Cu is shown in qualitative compositional images (Figure 14), in which their high and low contents display crustiform micro-bands. In Figure 14, high In and Cu contents correspond to low Zn contents, which thus supports the substitution mechanism above. In contrast, the Fe distribution in Figure 14 does not show any apparent zonal correlation with In, Cu, or Zn. Cd does not correlate with any of the analyzed elements and its contents in sphalerite from the three mines are mostly below 0.010 a.p.f.u., with the exception of peak Cd contents in the Chocaya mine (up to 1.25 Cd p.f.u.). The analyses are roughly arranged along the Zn + Cd = 1 line in Figure 13, thus suggesting punctual Zn ↔ Cd simple substitutions.

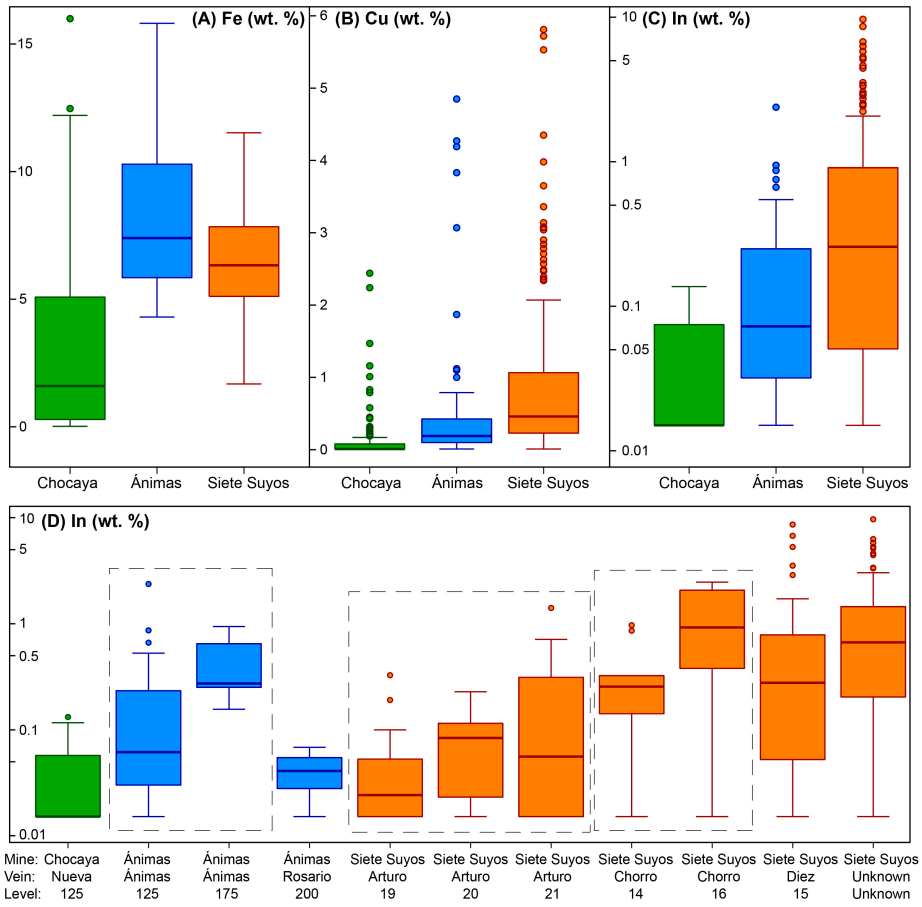

Figure 12. Box plot comparison of the Fe (**A**), Cu (**B**), and In (**C**) contents (wt.%) in sphalerite grains from the different mines and of In (wt.%) from the different veins and mining levels (**D**) studied in the Ánimas–Chocaya–Siete Suyos district. The central box is in the middle 50% of the data. The line in the box represents the median value for each box. Circles represent outliers, which are further than 1.5*(75th percentile/top of box-25th percentile/bottom of box) and the whiskers are the extreme values that are not outliers. For In, values below its detection limit (i.e., 0.03 wt.%) have been replaced by 0.015 wt.% to allow logarithmic scale axis in diagrams (**C**) and (**D**).

Most of the studied homogeneous, pristine sphalerite crystals plot within the sphalerite–stannite–roquesite pseudoternary system [25,77], similar to sphalerite from the Huari Huari deposit [39] (Figure 15). Most sphalerite analyses from the Ánimas–Chocaya–Siete Suyos deposits are distributed along the sphalerite–stannite and sphalerite–roquesite tie-lines in the Zn + Fe + Cd + Mn *vs*. Cu + Ag *vs*. Sn + In ternary diagram (Figure 15). The studied sphalerite samples contain up to 4.1 mol. % Cu_2FeSnS_4 (i.e., solid solution with stannite) and up to 9.1 mol. % $CuInS_2$ (i.e., solid solution with roquesite). A single analysis of a sphalerite grain from the Siete Suyos mine plotted along the sphalerite–chalcopyrite tie-line (Figure 15).

The wurtzite crystals were analyzed in surface samples from the Siete Suyos mine area (sample 1394). These analyses reveal variable concentrations of In that range between values below its detection limit and 1.61 wt.% in sphalerite grains with Fe concentrations that range between 1.23 and 5.29 wt.%. The concentrations of other cations, such as Cu (0.04 to 2.44 wt.%), Cd (0.65 to 1.26 wt.%), Sn (0.02 to 1.87 wt.%), and Ag (below the detection limit to 0.79 wt.%), are also variable. Germanium contents are systematically below its detection limit. The current wealth of data is not yet sufficient to draw clear cationic correlations between minor elements within wurtzite.

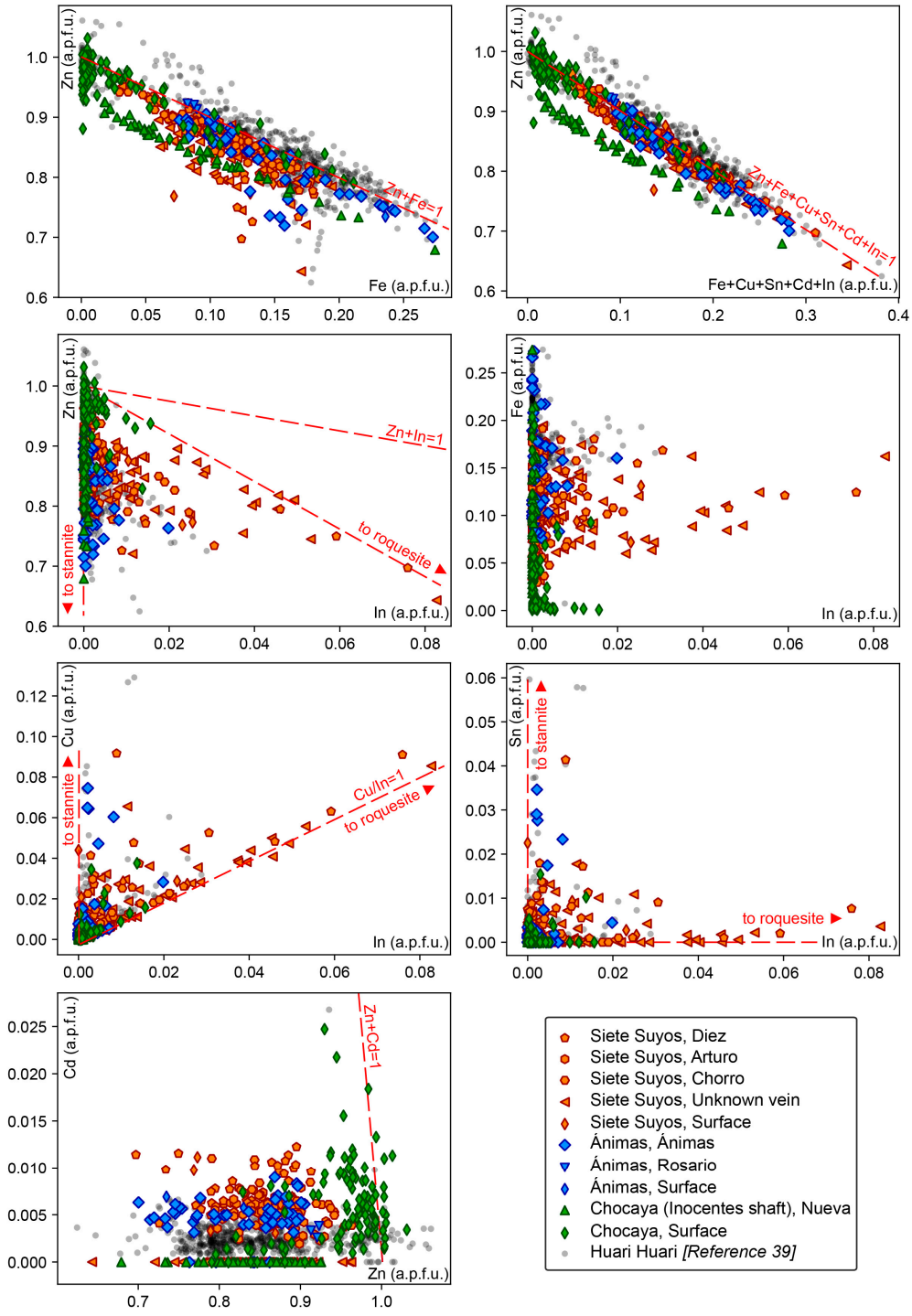

Figure 13. Correlation between elements in sphalerite from the Ánimas–Chocaya–Siete Suyos district. The chemical composition of sphalerite grains from the Huari Huari deposit is shown for comparison [39].

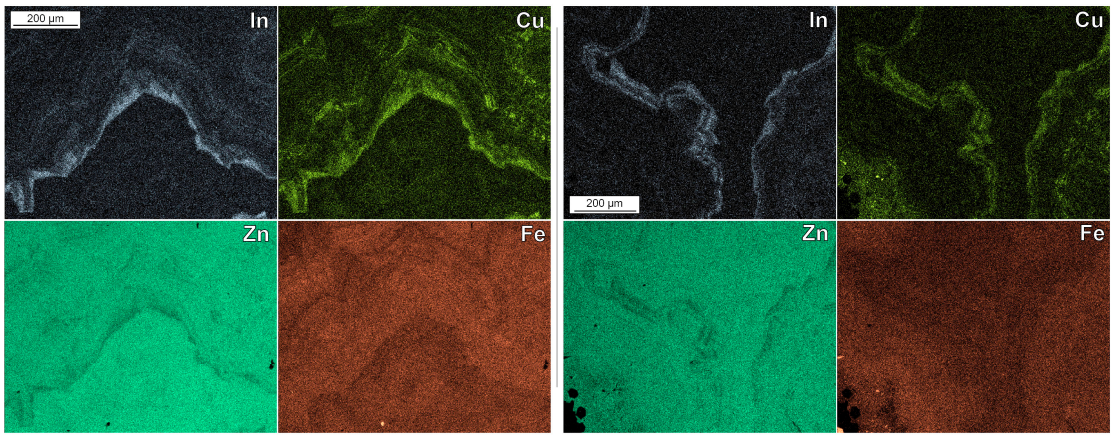

Figure 14. SEM-EDS qualitative X-ray images of In ($L\alpha$), Cu ($K\alpha$), Zn ($K\alpha$) and Fe ($K\alpha$) in sphalerite from the Diez vein in the Siete Suyos mine. Brighter colors indicate higher concentrations of the analyzed element. SEM-BSE images of the mapped areas are shown in Figure 5B (left group of compositional images) and Figure 5C (right group of compositional images).

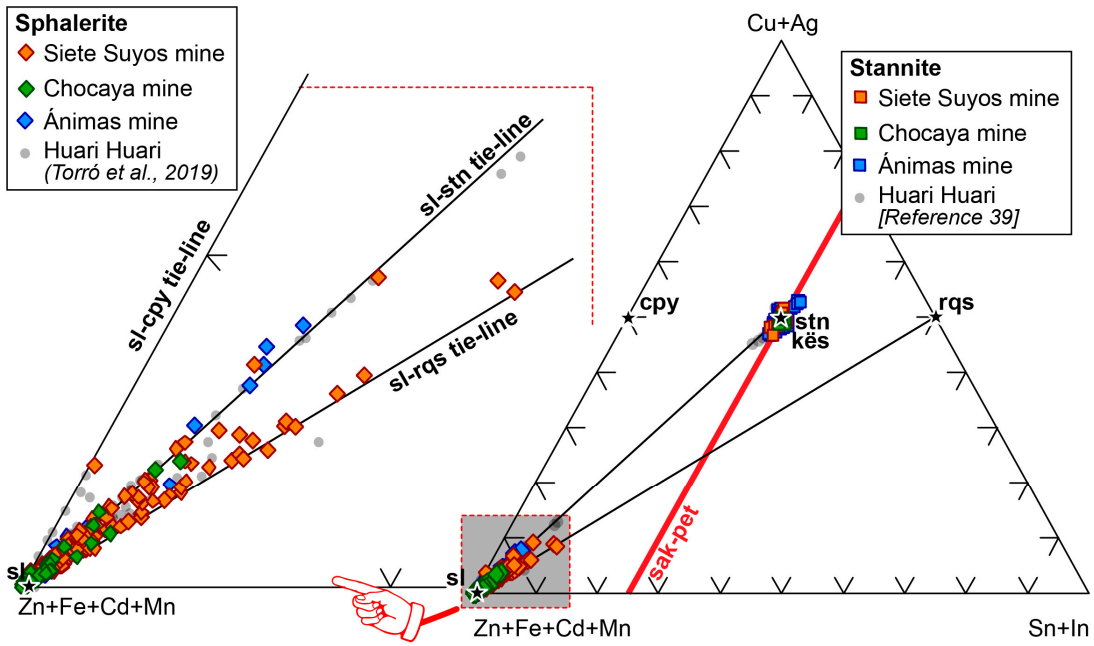

Figure 15. Plot of the analyzed sphalerite and stannite grains from the Ánimas–Chocaya–Siete Suyos district in the Zn + Fe + Cd + Mn vs. Cu + Ag vs. Sn + In ternary diagram. The composition of mineral end-members of interest is also plotted, and includes chalcopyrite (cpy), këstérite (kës), roquesite (rqs), sphalerite (sl) and stannite (stn). The compositional variation of sakuraiite (sak) and petrukite (pet) is also shown (bold, red line). The chemical composition of sphalerite and stannite grains from the Huari Huari deposit is shown for comparison [39].

Table 1. Summary of element concentrations in sphalerite from the Ánimas–Chocaya–Siete Suyos district (electron probe microanalysis data).

Mine	Vein	Wt.%	S	Zn	Fe	Cu	Sn	Cd	Ag	In	Ge
		d.l.	0.01	0.03	0.02	0.02	0.04	0.08	0.06	0.03	0.02
Entire district (n = 425)		MIN	31.70	42.80	0.02	b.d.l.	b.d.l.	b.d.l.	b.d.l.	b.d.l.	b.d.l.
		MAX	34.39	67.50	15.99	5.81	4.90	2.82	3.09	9.66	0.07
		Av.	33.04	58.76	5.49	0.56	0.25	0.46	0.04	0.50	0.00
Ánimas mine	All samples (n = 56)	MIN	32.01	47.55	4.30	b.d.l.	b.d.l.	b.d.l.	b.d.l.	b.d.l.	b.d.l.
		MAX	34.34	61.51	15.81	4.85	4.21	1.04	0.83	2.37	0.04
		Av.	33.20	56.08	8.35	0.62	0.40	0.54	0.05	0.21	0.00
	Surface (n = 2)	MIN	33.29	49.88	9.40	b.d.l.	b.d.l.	0.68	b.d.l.	b.d.l.	b.d.l.
		MAX	33.61	56.89	13.68	0.10	b.d.l.	0.81	b.d.l.	0.05	b.d.l.
		Av.	33.45	53.39	11.54	0.05	-	0.74	-	0.02	-
	Ánimas vein (n = 51)	MIN	32.01	47.55	4.30	b.d.l.	b.d.l.	b.d.l.	b.d.l.	b.d.l.	b.d.l.
		MAX	34.34	60.36	15.81	4.85	4.21	1.04	0.83	2.37	0.04
		Av.	33.22	55.89	8.43	0.67	0.43	0.54	0.05	0.23	0.00
	Ánimas vein, level 125 (n = 42)	MIN	32.39	47.55	4.30	b.d.l.	b.d.l.	b.d.l.	b.d.l.	b.d.l.	b.d.l.
		MAX	34.34	60.36	15.81	1.87	0.89	1.04	0.19	2.37	0.04
		Av.	33.28	56.33	8.70	0.25	0.11	0.53	0.02	0.20	0.00
	Ánimas vein, level 175 (n = 7)	MIN	32.01	48.15	4.84	0.54	0.24	0.43	b.d.l.	0.16	b.d.l.
		MAX	33.47	59.11	9.77	4.85	4.21	0.76	0.83	0.94	b.d.l.
		Av.	32.87	52.07	7.80	3.12	2.36	0.59	0.25	0.45	-
	Ánimas vein, level 200 (n = 2)	MIN	33.09	59.79	4.78	0.79	0.26	0.37	b.d.l.	0.11	b.d.l.
		MAX	33.13	60.17	4.79	1.00	0.45	0.60	b.d.l.	0.12	b.d.l.
		Av.	33.11	59.98	4.79	0.90	0.35	0.48	-	0.11	-
	Rosario vein, level 200 (n = 3)	MIN	32.46	60.95	4.69	0.02	0.04	0.30	b.d.l.	b.d.l.	b.d.l.
		MAX	32.74	61.51	5.11	0.10	0.06	0.44	b.d.l.	0.07	b.d.l.
		Av.	32.63	61.14	4.91	0.06	0.05	0.37	-	0.04	-
Chocaya mine	All samples (n = 149)	MIN	31.78	46.34	0.02	b.d.l.	b.d.l.	b.d.l.	b.d.l.	b.d.l.	b.d.l.
		MAX	34.39	67.50	15.99	2.44	1.87	2.82	0.79	1.82	0.03
		Av.	32.92	61.60	3.02	0.12	0.05	0.48	0.03	0.11	0.00
	Surface (n = 106)	MIN	31.78	53.45	0.02	b.d.l.	b.d.l.	b.d.l.	b.d.l.	b.d.l.	b.d.l.
		MAX	34.39	67.50	12.20	2.44	1.87	2.82	0.79	1.82	0.03
		Av.	32.78	63.31	2.18	0.15	0.06	0.67	0.03	0.14	0.00
	Nueva vein, 125 level (n = 43)	MIN	32.70	46.34	1.03	b.d.l.	b.d.l.	n.a.	b.d.l.	b.d.l.	n.a.
		MAX	33.76	62.05	15.99	0.21	0.27	n.a.	0.28	0.13	n.a.
		Av.	33.24	57.40	5.08	0.02	0.02	-	0.03	0.03	-
Siete Suyos mine	All samples (n = 220)	MIN	31.70	42.80	1.68	b.d.l.	b.d.l.	b.d.l.	b.d.l.	b.d.l.	b.d.l.
		MAX	34.32	63.79	11.52	5.81	4.90	1.41	3.09	9.66	0.07
		Av.	33.08	57.51	6.44	0.85	0.34	0.44	0.04	0.83	0.00
	Surface (n = 13)	MIN	32.04	50.77	4.13	0.19	0.13	0.35	b.d.l.	b.d.l.	b.d.l.
		MAX	33.31	60.39	8.45	2.84	2.72	1.26	0.26	2.94	0.07
		Av.	32.75	57.22	5.97	1.10	0.66	0.68	0.08	0.67	0.01
	Arturo vein (n = 59)	MIN	32.34	53.21	2.97	b.d.l.	b.d.l.	b.d.l.	b.d.l.	b.d.l.	b.d.l.
		MAX	33.91	63.08	10.78	1.96	1.70	0.92	3.09	1.41	b.d.l.
		Av.	33.25	58.38	6.89	0.27	0.15	0.58	0.08	0.13	-
	Arturo vein, 19 level (n = 16)	MIN	32.46	53.21	4.92	0.18	b.d.l.	0.48	b.d.l.	b.d.l.	b.d.l.
		MAX	33.64	60.62	8.48	0.70	0.62	0.73	3.09	0.33	b.d.l.
		Av.	33.04	57.96	7.16	0.40	0.28	0.62	0.21	0.05	-
	Arturo vein, 20 level (n = 16)	MIN	32.34	54.16	3.07	b.d.l.	b.d.l.	0.31	b.d.l.	b.d.l.	b.d.l.
		MAX	33.91	62.58	10.25	0.38	0.25	0.91	0.26	0.23	b.d.l.
		Av.	33.28	58.53	6.75	0.15	0.09	0.58	0.02	0.08	-
	Arturo vein, 21 level (n = 27)	MIN	32.57	54.03	2.97	b.d.l.	b.d.l.	b.d.l.	b.d.l.	b.d.l.	b.d.l.
		MAX	33.80	63.08	10.78	1.96	1.70	0.92	0.43	1.41	b.d.l.
		Av.	33.35	58.55	6.80	0.27	0.12	0.55	0.03	0.22	-

d.l.: detection limit. b.d.l.: below detection limit. n.a.: not analyzed. MIN: minimum value. MAX: maximum value. Av.: average value.

Table 1. Continuation.

		Wt.%	S	Zn	Fe	Cu	Sn	Cd	Ag	In	Ge
		d.l.	0.01	0.03	0.02	0.02	0.04	0.08	0.06	0.03	0.02
Siete Suyos mine	Chorro vein (n = 18)	MIN	32.29	52.59	1.68	0.22	0.00	0.43	0.00	0.00	0.00
		MAX	33.01	63.47	8.95	1.63	1.27	1.26	0.34	2.47	0.00
		Av.	32.69	59.91	4.10	0.78	0.33	0.76	0.06	0.72	0.00
	Chorro vein, 14 level (n = 9)	MIN	32.31	56.78	1.92	0.22	0.05	0.43	0.00	0.00	0.00
		MAX	33.01	63.47	6.94	1.45	1.27	1.26	0.12	0.97	0.00
		Av.	32.69	61.29	3.44	0.56	0.30	0.68	0.02	0.35	0.00
	Chorro vein, 16 level (n = 9)	MIN	32.29	52.59	1.68	0.28	0.00	0.57	0.00	0.00	0.00
		MAX	32.97	62.65	8.95	1.63	0.98	1.26	0.34	2.47	0.00
		Av.	32.69	58.53	4.75	0.99	0.36	0.84	0.10	1.10	0.00
	Diez vein, 15 level (n = 46)	MIN	31.70	45.07	4.40	0.00	0.00	0.25	0.00	0.00	0.00
		MAX	33.57	61.39	11.00	5.81	4.90	1.41	0.25	8.62	0.00
		Av.	32.79	55.71	7.15	1.19	0.59	0.85	0.04	0.91	0.00
	Unknown vein (n = 84)	MIN	31.70	42.80	1.72	0.00	0.00	0.00	0.00	0.00	0.00
		MAX	34.32	63.79	11.52	5.53	2.20	0.00	0.26	9.66	0.00
		Av.	33.24	57.41	6.31	1.06	0.29	0.00	0.01	1.32	0.00

d.l.: detection limit. b.d.l.: below detection limit. n.a.: not analyzed. MIN: minimum value. MAX: maximum value. Av.: average value.

Stannite-group minerals were analyzed in samples from the Ánimas, Chocaya and Siete Suyos mines, and a summary of their compositions is shown in Table 2. Only one stannite crystal from the Chocaya mine, in which this mineral occurs in trace amounts, was analyzed. The concentrations of Cu and Sn are relatively homogeneous and adjust to 2 and 1 a.p.f.u., respectively (Figure 16). In contrast, their Fe and Zn contents are variable, with Zn concentrations as high as 3.89 wt.% and Zn/(Fe + Zn) atomic proportions that range between 63.0 and 74.1. Atomic proportions of Fe and Zn yield a negative correlation, and most of the analyses arrange along the Fe + Zn = 1 line in the Zn *vs*. Fe (a.p.f.u.) diagram (Figure 16), thus pointing to a direct substitution between them (Fe ↔ Zn) that is probably framed in the stannite–kësterite solid solution series [78]. Stannite group minerals are up to 3.12 wt.% Ag (average = 0.40 wt.%), 2.16 wt.% Sb and 0.14 wt.% Ge, even though most of the values for Sb and Ge are normally below their respective detection limits. None of these elements yield clear correlations with other cations. Indium, which is up to 4.11 wt.% in stannite, yields no correlation with Fe or Zn, but it shows fair negative correlations with both Cu (at Cu + In = 2 a.p.f.u.) and Sn (at Sn + In = 1 a.p.f.u.; Figure 16). This suggests that the incorporation of In within the structure of stannite group minerals in this study is framed in the stannite-roquesite solid solution (Figure 15). The concentration of In in stannite does not show clear distribution trends, not even at different depths within single veins (Figure 17).

The chemical composition of cassiterite was analyzed in the samples from the Siete Suyos and Ánimas mines. FeO contents in cassiterite range between the 0.01 and 3.76 wt.% (average = 0.86 wt.%), SiO_2 contents range between below its detection limit and 0.18 wt.% (average = 0.10 wt.%), and MnO contents fall systematically below its detection limit. Ta_2O_5 and Nb_2O_5 contents mostly fall below their respective detection limits, except for peak values as high as 0.28 wt.% Ta_2O_5 and 0.13 wt.% Nb_2O_5. Indium concentrations are mostly above its detection limit and they are up to 0.25 wt.% In_2O_3 (average = 0.12 wt.% In_2O_3).

Table 2. Summary of element concentrations in stannite from the Ánimas–Chocaya–Siete Suyos district (electron probe microanalysis data).

Mine	Vein	Wt.% d.l.	S 0.01	Cu 0.02	Sn 0.04	Fe 0.02	Zn 0.03	Sb 0.04	Ag 0.06	In 0.03	Ge 0.02
Entire district (n = 157)		MIN	27.22	26.96	22.64	9.25	b.d.l.	b.d.l.	b.d.l.	b.d.l.	b.d.l.
		MAX	30.15	30.07	28.39	13.91	3.89	2.16	3.12	4.11	0.14
		Av.	29.19	28.61	26.93	11.13	2.13	0.10	0.40	0.59	0.00
Ánimas mine	All samples (n = 135)	MIN	27.22	26.96	22.64	9.25	b.d.l.	b.d.l.	b.d.l.	b.d.l.	b.d.l.
		MAX	30.15	30.07	28.26	13.05	3.89	2.16	3.12	4.11	0.14
		Av.	29.16	28.63	26.87	11.14	2.11	0.10	0.38	0.64	0.00
	Surface (n = 5)	MIN	28.75	28.35	26.60	12.69	0.47	b.d.l.	0.15	b.d.l.	b.d.l.
		MAX	29.62	28.96	27.72	13.05	1.74	b.d.l.	0.33	0.21	b.d.l.
		Av.	29.27	28.68	27.06	12.86	1.19	-	0.23	0.10	-
	Ánimas vein (n = 65)	MIN	27.22	27.34	25.16	9.25	b.d.l.	b.d.l.	b.d.l.	b.d.l.	b.d.l.
		MAX	30.15	30.07	28.26	12.75	3.05	0.57	1.02	2.31	0.14
		Av.	29.17	28.65	27.01	11.42	1.60	0.02	0.25	0.61	0.01
	Ánimas vein, 100 level (n = 24)	MIN	28.58	27.59	25.16	9.25	b.d.l.	b.d.l.	b.d.l.	0.15	b.d.l.
		MAX	29.82	30.07	27.78	12.75	2.99	0.57	1.02	2.31	0.14
		Av.	29.33	28.77	26.85	11.08	1.60	0.05	0.23	0.75	0.02
	Ánimas vein, 125 level (n = 1)	Value	29.28	28.19	26.70	11.39	2.45	b.d.l.	0.51	0.71	b.d.l.
	Ánimas vein, 175 level (n = 8)	MIN	29.51	28.53	26.91	10.79	1.47	b.d.l.	b.d.l.	b.d.l.	b.d.l.
		MAX	29.87	29.14	28.26	12.39	2.72	0.16	0.44	0.30	b.d.l.
		Av.	29.65	28.83	27.72	11.49	1.93	0.03	0.23	0.12	-
	Ánimas vein, 200 level (n = 32)	MIN	27.22	27.34	25.33	10.16	b.d.l.	b.d.l.	b.d.l.	0.06	b.d.l.
		MAX	30.15	29.91	28.14	12.59	3.05	0.05	0.56	1.64	b.d.l.
		Av.	28.92	28.52	26.97	11.66	1.49	0.00	0.27	0.62	-
	Burton vein, 232 level (n = 21)	MIN	28.57	27.35	22.64	9.90	1.62	b.d.l.	b.d.l.	0.18	b.d.l.
		MAX	29.55	29.28	27.66	11.96	3.89	2.16	3.12	4.11	b.d.l.
		Av.	29.09	28.60	26.60	10.98	2.24	0.25	0.56	0.83	-
	Colorada vein, (n = 33)	MIN	28.50	27.51	24.79	9.42	1.67	b.d.l.	b.d.l.	0.15	b.d.l.
		MAX	30.00	29.35	27.96	12.84	3.88	1.54	2.74	1.81	0.04
		Av.	29.21	28.67	26.68	10.25	3.24	0.21	0.52	0.74	-
	Colorada vein, 264 level, (n = 16)	MIN	28.50	27.51	24.87	9.42	2.79	b.d.l.	0.16	0.36	n.a.
		MAX	29.07	29.35	27.31	10.76	3.56	1.54	2.74	1.81	n.a.
		Av.	28.89	28.30	26.13	10.15	3.16	0.25	0.75	1.08	-
	Colorada vein, 302 level, (n = 17)	MIN	28.50	28.44	24.79	9.63	1.67	b.d.l.	b.d.l.	0.15	b.d.l.
		MAX	30.00	29.27	27.96	12.84	3.88	0.96	0.76	1.70	0.04
		Av.	29.51	29.03	27.19	10.35	3.31	0.17	0.30	0.42	0.00
	Rosario vein, 200 level, (n = 11)	MIN	28.79	26.96	25.18	10.65	1.19	b.d.l.	0.31	0.07	b.d.l.
		MAX	29.32	29.13	27.97	12.82	2.62	b.d.l.	0.85	2.10	b.d.l.
		Av.	29.12	28.51	27.07	11.61	1.91	-	0.49	0.48	-
Chocaya mine	Surface (n = 1)	Value	29.70	28.91	27.02	10.32	3.21	0.14	0.67	0.29	b.d.l.
Siete Suyos mine	All samples (n = 21)	MIN	28.27	26.99	25.41	10.03	b.d.l.	b.d.l.	b.d.l.	b.d.l.	b.d.l.
		MAX	29.83	29.05	28.39	13.91	3.73	1.27	2.87	1.73	b.d.l.
		Av.	29.36	28.41	27.30	11.16	2.20	0.11	0.53	0.27	b.d.l.
	Surface (n = 19)	MIN	28.67	27.44	25.64	10.03	1.25	b.d.l.	b.d.l.	b.d.l.	0.00
		MAX	29.83	29.05	28.39	11.88	3.73	1.27	2.87	0.73	0.00
		Av.	29.41	28.54	27.46	10.97	2.28	0.12	0.53	0.21	0.00
	Diez vein, level 15 (n = 1)	Value	29.48	27.47	26.04	12.00	2.80	b.d.l.	0.44	1.73	b.d.l.

d.l.: detection limit. b.d.l.: below detection limit. n.a.: not analyzed. MIN: minimum value. MAX: maximum value. Av.: average value.

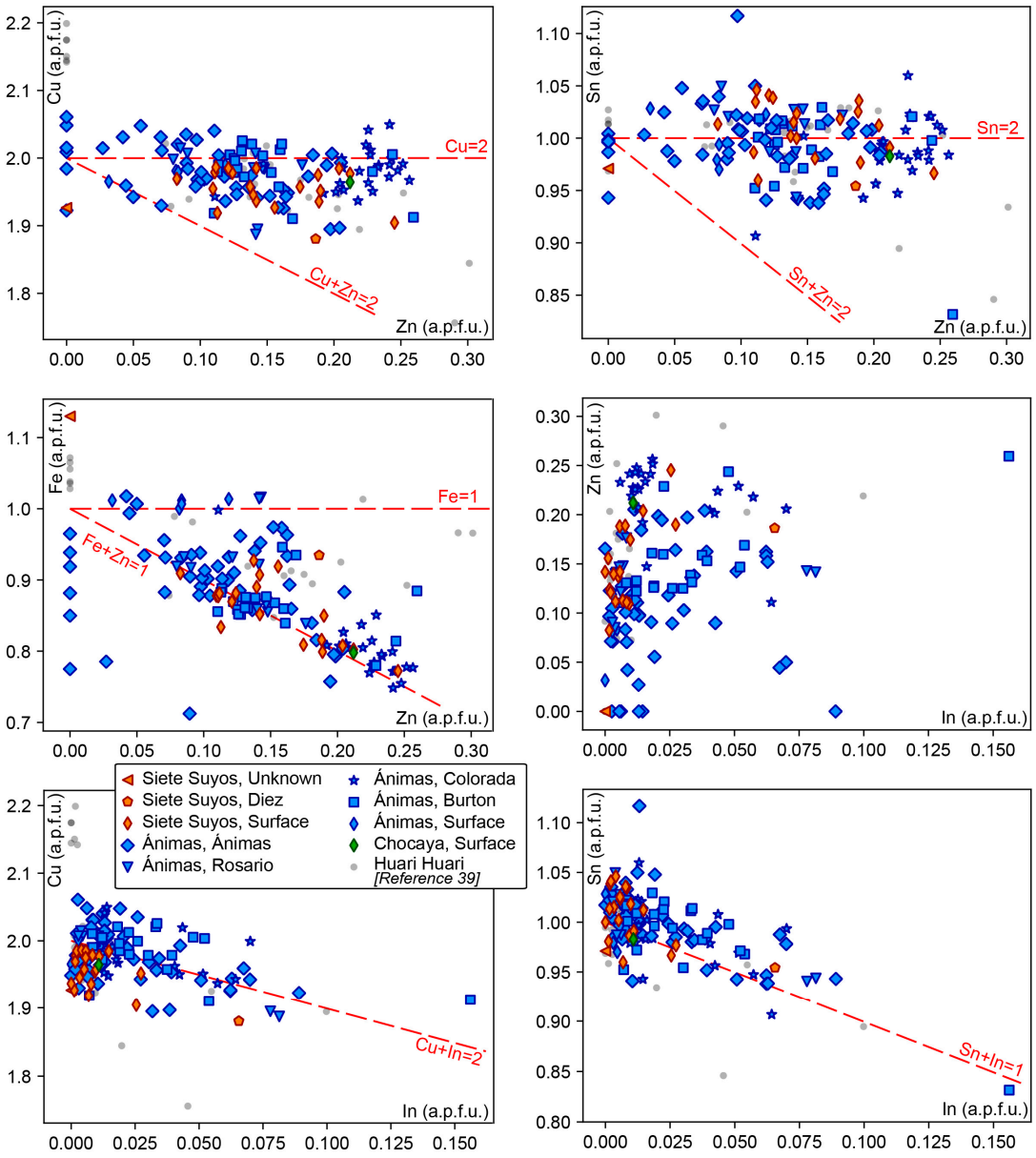

Figure 16. Correlation between elements in stannite from the Ánimas–Chocaya–Siete Suyos district. The chemical composition of stannite grains from the Huari Huari deposit is shown for comparison [39].

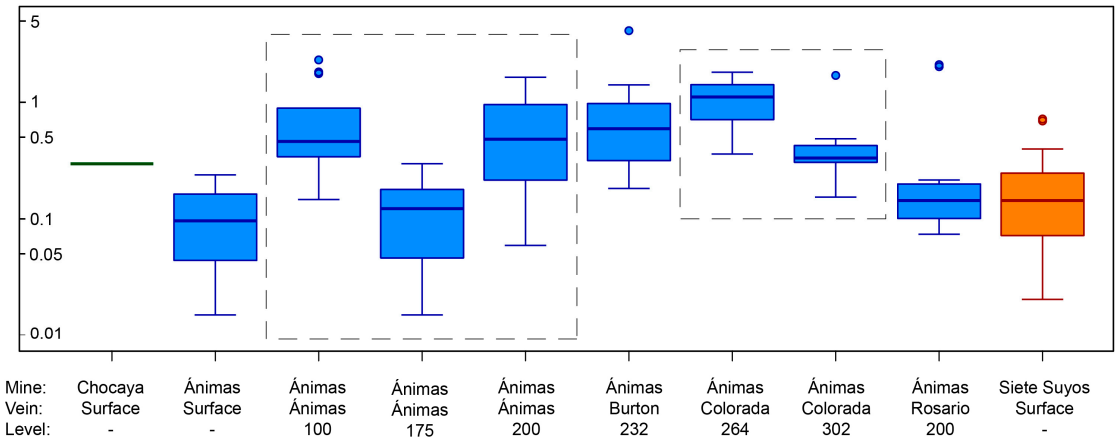

Figure 17. Box plot comparison of In contents (wt.%) in stannite from the different mines, veins and mining levels studied in the Ánimas–Chocaya–Siete Suyos district. The central box is in the middle 50% of the data. The line in the box represents the median value for each box. The outliers are further than 1.5×(75th percentile/top of box-25th percentile/bottom of box) and the whiskers are the extreme values that are not outliers. Values below the detection limit (i.e., 0.03 wt.%) have been replaced by 0.015 wt.% to allow for logarithmic scale axis plotting.

5.2. Other Minerals

Other minerals whose mineral chemistry was analyzed are arsenopyrite, wolframite, galena, tetrahedrite-group minerals, and a variety of other sulfosalts in minor amounts, (i.e. semseyite, boulangerite, jamesonite, franckeite, miargyrite, pyrargyrite, andorite, aramayoite, diaphorite, fizélyite, staročeskéite, terrywallaceite, oscarkempffite, and ramdohrite). In all of them, their concentrations in critical metals In and Ge were systematically below their respective detection limits.

Arsenopyrite was analyzed in the vein samples from Ánimas and Burton veins in the Ánimas mine. Analyzed grains from both veins yield overlapping As contents that range between 29.8 and 31.5 at.%, and S contents that range between 35.5 and 35.6 at.%. Sb contents range between 0.74 and 0.89 at.%, and Ni and Co contents are up to 0.03 and 0.06 at.%, respectively.

Wolframite was analyzed in samples from the Ánimas mine. The analyzed grains include ferberite (FeO between 19.31 and 22.12 wt.% and MnO between 0.50 and 3.24 wt.%) and less abundant hübnerite (FeO between 0.03 and 7.77 wt.% and MnO between 16.04 and 22.93 wt.%).

Galena was analyzed in the samples from the Ánimas vein in the Ánimas mine, from the Chorro vein and the surface in the Siete Suyos mine, and from the Nueva vein and the surface at the Chocaya mine. Analyzed galena grains yield extremely variable Pb contents, which range between 75.47 and 87.39 wt.%. The Pb contents are inversely correlated with those of Sb (0.07 to 8.70 wt.%), Sn (b.d.l. to 0.61), Zn (b.d.l. to 4.46 wt.%), and Bi (b.d.l. to 6.17 wt.%). The Ag contents are also variable, but are, in general, higher in the Ánimas mine (up to 3.02 wt.%) than in the Siete Suyos (up to 0.69 wt.%) and Chocaya (up to 0.11 wt.%) mines. The Ge contents in galena are up to 0.17 wt.% in the Siete Suyos mine, up to 0.15 wt.% in the Chocaya mine, and up to 0.17 wt.% in the Ánimas mine, and average 0.11 wt.% at a district scale.

Tetrahedrite group minerals were analyzed in the samples from the Ánimas and Siete Suyos mines. They belong to the tetrahedrite and freibergite species (Figure 18). Arsenic contents are systematically very low, mostly below its detection limit and up to 0.70 wt.%, which results in very low As/(As + Sb) ratios between 0 and 0.04 (atomic proportions). Silver is up to 32.3 wt.%, and its concentration is variable in analyzed grains from both mines; however, tetrahedrite-group minerals in the Siete Suyos mine are, in general, richer in silver (average = 25.41 wt.% Ag) than in the Ánimas mine (average = 18.69 wt.% Ag; Figure 18). The Ag/(Ag + Cu) ratio ranges between 0.21 and 0.56 (atomic proportions) and, accordingly, correspond to freibergite (Ag/(Ag + Cu) > 0.5) and argentian tetrahedrite (Figures 18 and 19). Zinc and Fe show variable concentrations in both of the mines. Iron contents (4.02 to 5.81 wt.%) are systematically higher than Zn contents (below its detection limit to

2.47 wt.%), and the Zn/(Zn + Fe) ratio ranges between 0.00 and 0.34 (atomic proportions). The concentrations of In, Ge, and Ga are systematically below their detection limits.

Semseyite, boulangerite, and jamesonite were analyzed in the Siete Suyos and Ánimas mines. Semseyite is up to 0.14 wt.% Ag (average = 0.06 wt.% Ag; n = 11) and up to 0.13 wt.% Ge (average = 0.04 wt.% Ge; n = 6). Boulangerite is up to 8.31 wt.% Ag (average = 4.30 wt.% Ag; n = 26) and up to 0.11 wt.% Ge (average = 0.03 wt.% Ge). However, such high Ag contents as of some of the analyses can be spurious due to mixed analyses of finely intergrown Pb and Sb sulfosalts (see Figures 3–5, 7–10). Jamesonite is up to 0.28 wt.% Ag, even though most of the analyses yield concentrations that are below the detection limit for this element, and up to 0.11 wt.% Ge (average = 0.04 wt.% Ge; n = 21).

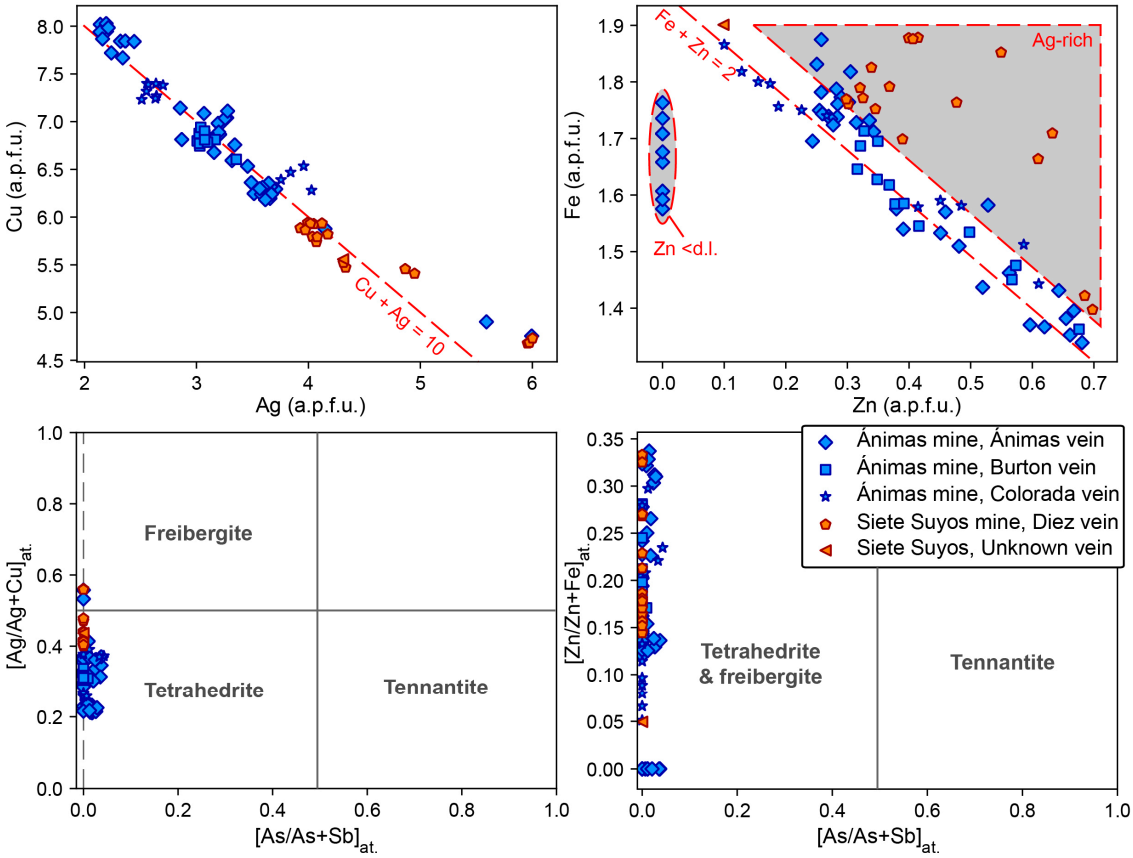

Figure 18. Correlation between elements in tetrahedrite-group minerals (tetrahedrite and freibergite) from the Ánimas–Chocaya–Siete Suyos district. The divergence of some compositions to values of Cu + Ag > 10 a.p.f.u. in the Ag vs. Cu diagram and of Fe + Zn > 2 in the Zn vs. Fe diagram is mainly attributable to cation normalization to S = 13 a.p.f.u., which results in an overestimation of the atomic proportion of the other elements in Ag-rich tetrahedrite and freibergite due to the S ↔ exchange.

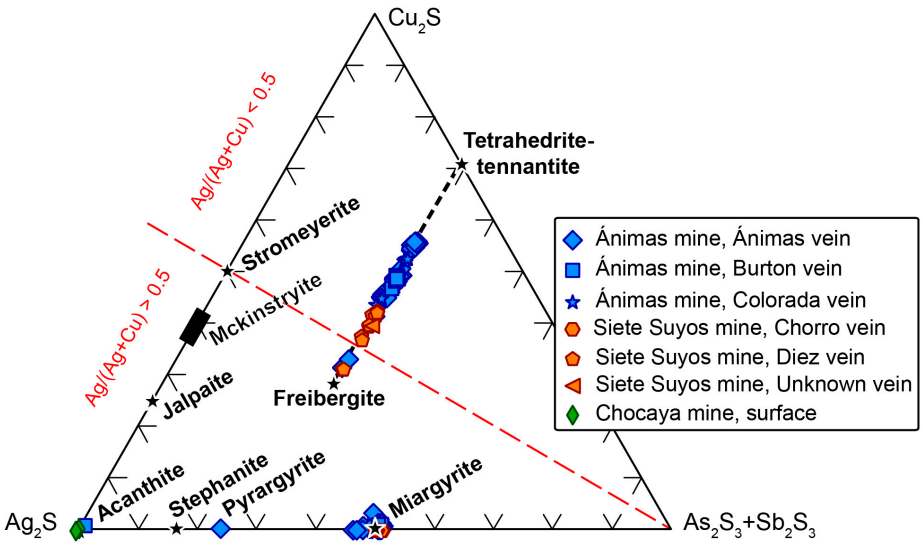

Figure 19. Plot of the analyzed tetrahedrite-group minerals and Ag–Cu–Sb sulfosalts from the Ánimas–Chocaya–Siete Suyos district in the Ag_2S vs. Cu_2S vs. Sb_2S_3 + As_2S_3 ternary diagram.

6. Discussion

6.1. Paragenetic Sequences and Evolution of the Mineralizing Fluids

The mineral sequences for each studied vein in the Siete Suyos, Ánimas, and Chocaya mines are diagrammatically shown in Figures 20–22. The described textures indicate a generalized early crystallization of cassiterite and arsenopyrite, along with variable proportions of quartz, which is the main and almost unique gangue mineral in all of the studied veins. Cassiterite is more abundant in the Ánimas mine than in the rest of the district, particularly in the Ánimas and Colorada veins, is only found as a minor mineral in the Siete Suyos mine and it is apparently absent in the Nueva vein from the Chocaya mine. Cassiterite is often replaced by sulfides, such as sphalerite and stannite, and sulfosalts. Such replacement is possibly the main reason for the variable concentrations of cassiterite in the Ánimas and Siete Suyos mines. This is illustrated, for instance, by the unusual higher abundance of cassiterite in shallow levels in the Ánimas vein, whereas stannite is far more abundant than cassiterite in the deeper levels (Figure 6).

Pyrite displays a variety of textural features that require special attention. The most common textural type of pyrite in the Ánimas, Chocaya, and Siete Suyos veins corresponds to anhedral shapes and secondary porosity that shows a recurrent orbicular to pseudo-hexagonal distribution—and infillings of hypogene (quartz, sphalerite, stannite-group minerals and sulfosalts; Figures 3B,C, 6A,D,K, 7C,D, 8A, 10D,E, 11A) or supergene minerals (e.g., angelellite; Figure 9K). In samples from the Arturo vein in the Siete Suyos mine, individual pyrite crystals with pseudo-hexagonal shapes (prior to corrosion, which results in engulfment) are frequent (Figure 3B,C). Fairly abundant are also pyrite grains in mm-sized garland-like aggregates along with cassiterite, arsenopyrite and quartz grains that draw circular to pseudo-hexagonal shapes with a central space that is mostly lined with quartz or sphalerite (Figures 3G, 9G, 11J). The recurrence in hexagonal patterns by pyrite and other minerals (e.g., galena and sulfosalts in Figure 4D) in veins from the three mines cannot therefore be considered as a mere anecdote. It strongly suggests a replacement that is either pseudomorphic or driven through particular planes of a former mineral with an original hexagonal or pseudo-hexagonal crystal shape. In Bolivian-type deposits, pyrrhotite is the most likely mineral that forms hexagonal crystals that are to be replaced by other sulfides, since it has been amply described to crystallize early in the mineralization sequence in different deposits (e.g. [33,39,62,63,66]). Pyrrhotite has indeed been observed in samples from the Nueva vein in the Chocaya mine as anhedral relicts and inclusions in pyrite–marcasite–intermediate product aggregates (Figure 11B,C,K). The presence of intergrown

pyrite, marcasite and intermediate product itself, and the generation of secondary porosity are solid arguments for their formation by alteration of pyrrhotite [75,76] by an increase in the state of sulfidation—a combination of temperature and fS_2 (e.g., [39]). Of particular interest for Bolivian-type deposits is the benchmark petrographic study of Kelly and Turneaure [66] that describes early hexagonal pyrrhotite, which is partly replaced by monoclinic pyrrhotine along the borders of pyrite–marcasite–siderite veinlets. The occurrence of hexagonal pyrrhotite would point to its crystallization under temperatures above 308 °C, which corresponds to the upper limit of formation for monoclinic pyrrhotite [75,79]. Atomic proportions of As in arsenopyrite crystals from the Ánimas and Burton veins indicate temperatures of crystallization, in equilibrium with pyrrhotite, which range between 288° and 389 °C [80], in good agreement with the crystallization temperatures constrained from the likely occurrence of hexagonal pyrrhotite. The absence of pyrrhotite in the studied veins from the Ánimas and Siete Suyos mines is interpreted, in this context, as the result of its total replacement by pyrite ± marcasite. Such a hypothesis would somehow imply that this replacement did not homogeneously occur throughout the district. Gradients in the degree of replacement of pyrrhotite by marcasite and pyrite along replacement fronts are described in detail in the "Cordilleran" polymetallic deposit of Cerro de Pasco in Peru [81]; similar to our observations and interpretation, these authors describe porous, fine-grained marcasite containing pyrrhotite relicts to mark the beginning of the replacement, which progressively grades to euhedral, nonporous pyrite that is devoid of pyrrhotite relicts. Following this scheme in the Ánimas–Chocaya–Siete Suyos district, the circulation of hydrothermal fluids leading to the replacement of pyrrhotite by pyrite and marcasite would be centered in veins in the NW zone (Siete Suyos mine: pyrite, without marcasite or pyrrhotite), and it was distal to veins in the SE zone (Chocaya mine: pyrite, marcasite, intermediate product, and relicts of pyrrhotite). A complete replacement of pyrrhotite by pyrite along the lifespan of mineralizing systems might lead to the erroneous interpretation that pyrite crystallized early in the sequence in some deposits along with cassiterite, as Ramdohr [75] warned.

In general, the crystallization of most of the sphalerite and stannite-group minerals in the Ánimas–Chocaya–Siete Suyos district followed the crystallization of pyrrhotite, cassiterite, and arsenopyrite (Figures 20–22). Iron contents in sphalerite vary broadly at the district scale and within individual veins. The conspicuous enrichment in iron above ~ 21 mol.% FeS in some sphalerite grains from the Ánimas (up to 27.7 mol.% FeS) and Nueva (up to 28.8 mol.% FeS) veins would point to crystallization in equilibrium with pyrrhotite at temperatures above 250 °C [82]. In contrast, the majority of the analyzed sphalerite grains yield FeS concentrations below ~21 mol.% that are compatible with the crystallization of sphalerite along with pyrrhotite + pyrite or with pyrite alone. Accordingly, we consider that Fe-rich (> 21 mol.% FeS) sphalerite grains in the Ánimas and Nueva veins were crystallized along with pyrrhotite, and sphalerite crystals with FeS < 21 mol.% in all veins crystallized in equilibrium with pyrite (Figures 20–22). Stannite-group minerals were generally deposited after sphalerite and they are dominated by stannite (± këserite) compositions. Local famatinite was only observed in one sample from the Rosario vein in the Ánimas mine (Figure 21). Finally, an "invasion" of galena and a wealth of Ag-Pb-Sn sulfosalts, which are characteristic of Bolivian-type deposits in general, and of the Ánimas and Chocaya mines in particular [83], occurs late in the sequence in all of the studied veins (Figures 20–22).

Three stages of mineralization have been identified in the Ánimas–Chocaya–Siete Suyos deposit (Figures 20–22). Assemblages that are typically found in low-sulfidation mineralization characterize stage 1 and include cassiterite, arsenopyrite, pyrrhotite, and high-Fe (FeS > 21 mol. %) sphalerite. Stage 2 comprises the crystallization of minerals typical of intermediate-sulfidation assemblages such as pyrite–marcasite, sphalerite (with FeS < 21 mol. %) and stannite-famatinite. Stage 3 is characterized by the crystallization of Ag-Pb-Sn sulfosalts, which are typical of intermediate-sulfidation mineralization [84–86]. Accordingly, ore mineralization in the Ánimas–Chocaya–Siete Suyos district registers a shift from low- to intermediate-sulfidation environments, similar to that described in other Bolivian-type deposits (e.g., [39]). Similar three-stage evolution of the mineralization systems has been described in porphyry-related epithermal base metal ("Cordilleran-type") deposits (e.g., [35,81]).

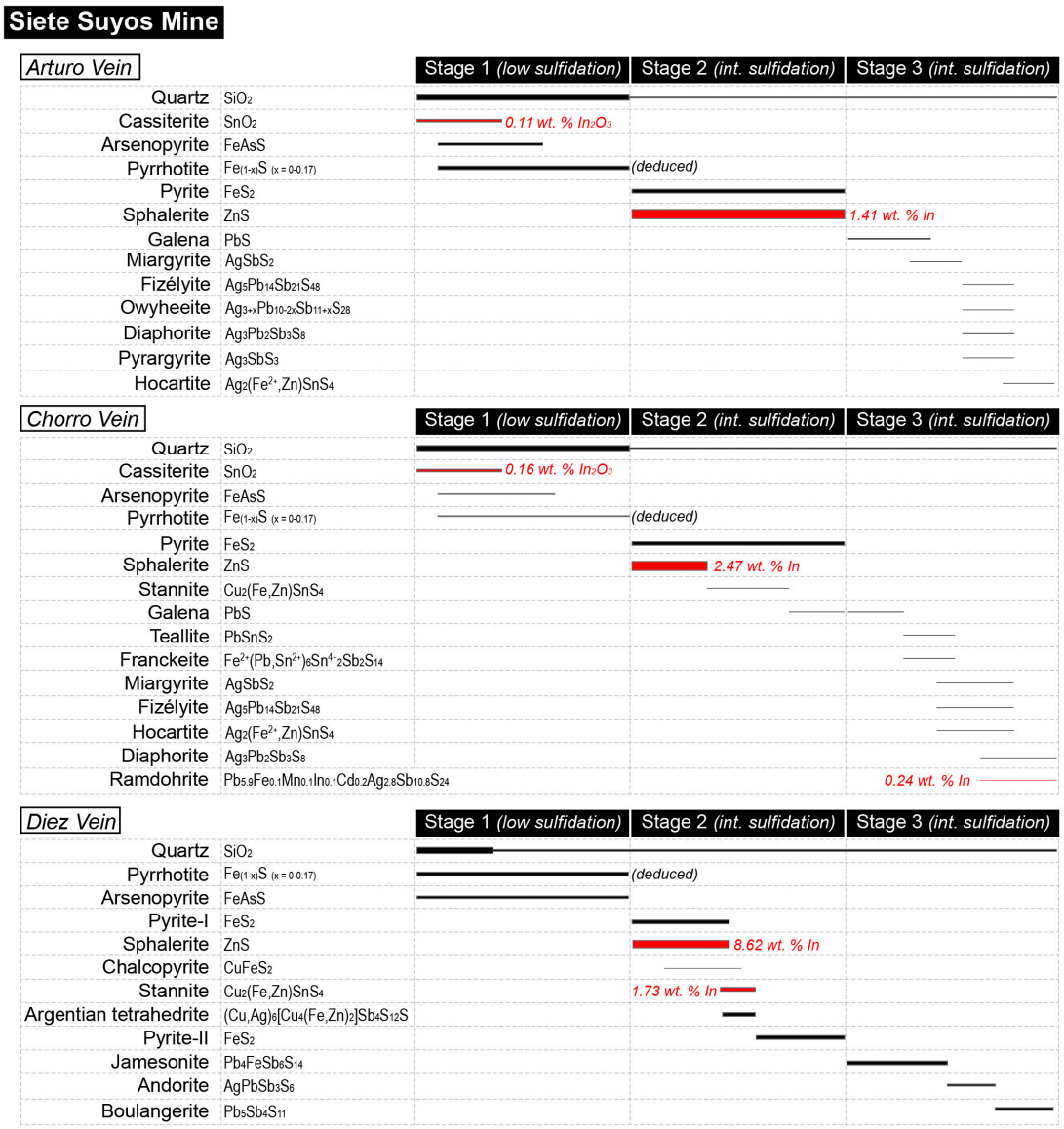

Figure 20. Paragenetic sequences deduced for the hypogene mineralization in the Arturo, Chorro and Diez veins in the Siete Suyos mine. The width of the bars approximates the relative abundance of the listed minerals. Location of the mineral phases or generations yielding highlighted concentrations of In and the maximum concentrations for this metal are indicated in red color. The timing of crystallization shown in the paragenetic sequence is relative to observations made on each vein, and therefore does not necessarily indicate absolute timing.

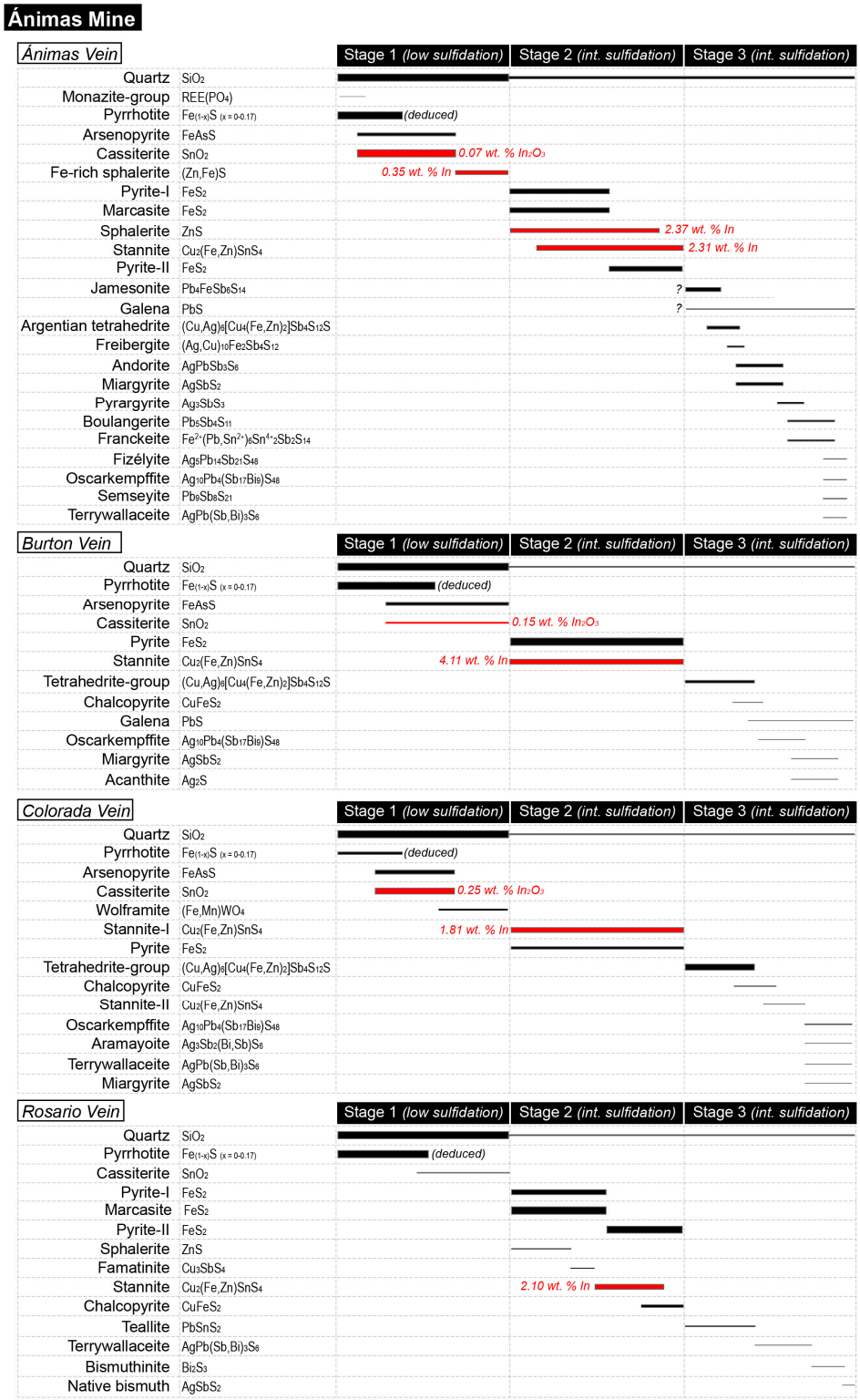

Figure 21. Paragenetic sequences deduced for the hypogene mineralization in the Ánimas, Burton, Colorada and Rosario veins in the Ánimas mine. The width of the bars approximates the relative abundance of the listed minerals. Location of the mineral phases or generations yielding highlighted concentrations of In and the maximum concentrations for this metal are indicated in red color. The timing of crystallization shown in the paragenetic sequence is relative to observations made on each vein, and therefore does not necessarily indicate absolute timing.

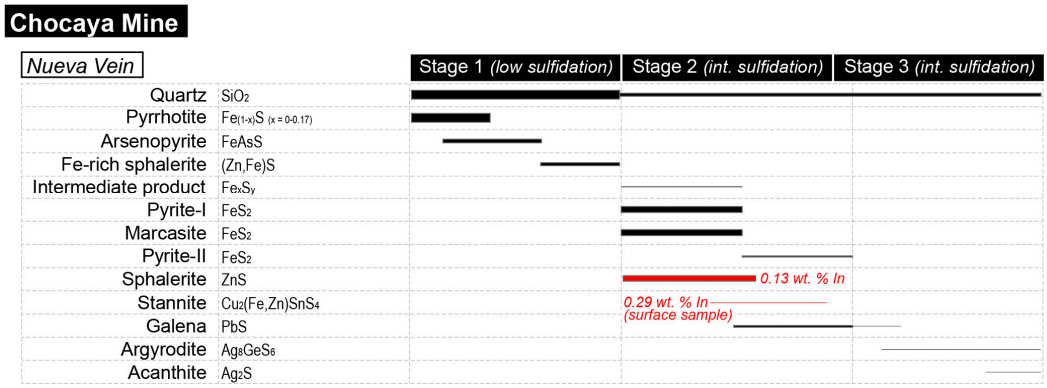

Figure 22. Paragenetic sequence deduced for the hypogene mineralization in the Nueva vein in the Chocaya mine. The width of the bars approximates the relative abundance of the listed minerals. Location of the mineral phases or generations yielding highlighted concentrations of In, and the maximum concentration for this metal are indicated in red color.

6.2. Indium: Mineralogical Expression and Controls on Its Distribution

Remarkable concentrations of In were chiefly detected in sphalerite and stannite, and also in wurtzite, cassiterite, and ramdohrite. Sphalerite, stannite and cassiterite are major constituents of the ore mineralization in the Ánimas–Chocaya–Siete Suyos district and they appear to host the majority of this critical metal in the district. The high concentration of In in these minerals represents the mineralogical expression of the high concentrations of In (up to 2510 ppm) in whole-ore chemical analyses that were reported by Ishihara et al. [37]. In underground samples, the highest concentrations of In in sphalerite are found in veins from the Ánimas and Siete Suyos mines, whereas the maximum values of In are relatively low in sphalerite from the Nueva vein in the Chocaya mine. A similar distribution pattern is shown in the isovalue map for maximum In concentration in sphalerite grains in the surface samples shown in Figure 23A. Regarding concentrations of In in stannite, the maximum values are found in underground and surface samples in the Ánimas mine, where stannite is more abundant (Figure 23B).

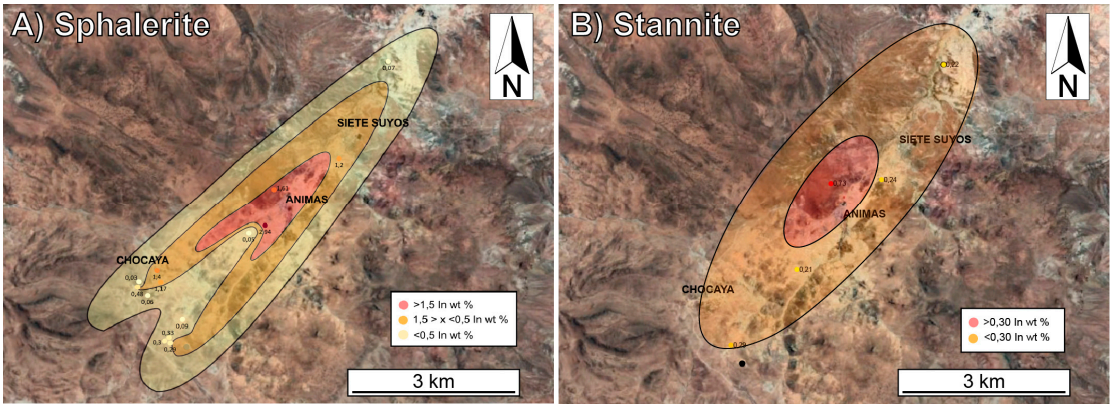

Figure 23. Isovalue maps for maximum concentrations of indium in sphalerite (**A**) and stannite (**B**) grains in surface samples from the Ánimas–Chocaya–Siete Suyos district. Google Earth satellite base image.

The incorporation of In in sphalerite and stannite can be contextualized in the sphalerite–stannite–roquesite pseudoternary system (Figure 15) [77,87,88]. In sphalerite grains from the Ánimas–Chocaya–Siete Suyos district, the roquesite component reaches 9.1 mol. %, which is well within the empirically stablished 60 mol. % maximum tetragonal $CuInS_2$ component in solid solution within cubic, sphalerite-type-structure ZnS [87,88]. The correlation that was observed between the

atomic concentrations of In and Cu in sphalerite at Cu/In = 1 (Figure 13) is in good agreement with the well documented incorporation of In in sphalerite following a $(Cu^{+} + In^{3+}) \leftrightarrow 2Zn^{2+}$ coupled substitution [11,12,25,39,89,90]. The prevalence (and apparent exclusivity) of this substitution mechanism for the incorporation of In in the structure of sphalerite makes the availability of Cu in the mineralizing system a key factor that controls the distribution and primary concentration of the critical metal. Therefore, it might be anticipated that high concentrations in In across a given deposit or district can only occur if sphalerite crystallized under relatively high activity of Cu. In the studied district, the highest concentrations and average values of In in sphalerite occur in the Siete Suyos mine, which also hosts sphalerite with the highest Cu contents (Figure 12). The occurrence of chalcopyrite disease texture is probably related with the distinctively high activity of Cu during the crystallization of In-rich sphalerite in the Diez vein from the Siete Suyos mine (Figure 5C,D). Such a texture was not observed in the other studied veins. In hydrothermal systems, chalcopyrite disease is mostly attributed to diffusion-controlled replacement of Fe by Cu or to co-crystallization of sphalerite and chalcopyrite [91]. The first case appears to be unlikely in the Diez vein since chalcopyrite disease texture is local and restricted to micro-bands that are not particularly enriched in Fe. X-ray element maps (Figure 14) indicate a compositional zoning in sphalerite characterized by alternating micro-bands enriched in both In and Cu and micro-bands depleted in these elements at relatively constant Fe contents. The crustiform morphologies that are depicted by such bands indicate that they formed as infillings of open spaces, and the alternate superposition of Cu + In-rich and -poor bands suggests the episodic entrainment of fluids enriched in Cu and In during the mineralization.

The substitution mechanism that allows for the incorporation of In in stannite is poorly understood. However, our data from the Ánimas–Chocaya–Siete Suyos district suggest that In enrichment is associated with Sn and Cu depletions, at Sn at Sn + In = 1 and Cu + In = 2 (Figure 16; see also [39]). In contrast, a petrukite $[(Cu,Zn,Fe)_3(In,Sn)S_4]$ component that accounts for the incorporation of In in the studied stannite grains is, in principle, ruled out, since the atomic contents of Cu do not show any correlation with those of Zn or Fe (Figure 16).

Iron did not play an obvious role in the enrichment of In in the Ánimas–Chocaya–Siete Suyos mineralization, as its atomic concentration in sphalerite does not correlate with that of In, and trends toward In enrichment are observed at any concentration of Fe (Figure 16). However, the Fe contents in sphalerite are indeed useful for the discrimination between sphalerite that crystallized in equilibrium with either pyrrhotite (stage 1) or pyrite (stage 2; Figures 20–22). It is noteworthy that sphalerite with In contents above 1.0 wt.% (54 out of a total 416 EPMA analyses) yielded FeS contents that were below 18 mol. %, thus pointing to crystallization in equilibrium with pyrite and, probably, out of the stability field of pyrrhotite [82]. In contrast, Fe-rich (FeS > 21 mol. %; stage-1) sphalerite yielded much lower In contents (up to 0.35 wt.% In at the Ánimas vein; Figure 21). In consequence, we deduce that the main incorporation of In in the Ánimas–Chocaya–Siete Suyos mineralization occurred during the crystallization of sphalerite and stannite in an intermediate-sulfidation stage of mineralization (stage 2 in Figures 20–22). In addition, the modest In enrichment in cassiterite and high-Fe sphalerite took place during an earlier low-sulfidation stage of mineralization (stage 1). Finally, ramdohrite, which crystallized late in the paragenetic sequence during an intermediate-sulfidation and sulfosalt-rich mineralization stage (stage 3), also accounts for some minor In contents.

7. Conclusions

Detailed textural observations in ore mineralization from the Ánimas–Chocaya–Siete Suyos district revealed a relatively complex mineralogy that can be associated with a three-stage mineralization sequence. In general terms, a first stage rich in cassiterite + arsenopyrite + pyrrhotite ± Fe-rich sphalerite was followed by a second stage rich in pyrite + sphalerite + stannite ± famatinite and a third stage rich in galena and Ag-Pb-Sn sulfosalts. The mineralogy records a shift from the low- to intermediate-sulfidation stages of mineralization. Intermediate-sulfidation assemblages are dominant in vein mineralization in the Ánimas and Siete Suyos mines, in the SE sector of the district.

Indium occurs in exceptionally high concentrations in sphalerite (up to 9.66 wt.% In) and stannite (up to 4.11 wt.% In) from the Ánimas and Siete Suyos mines, and in lower, although still anomalous, amount in wurtzite (up to 1.61 wt.% In), cassiterite (up to 0.25 wt.% In_2O_3), and ramdohrite (up to 0.24 wt.% In).

In sphalerite, the atomic concentrations of In and Cu yield positive correlations at Cu/In = 1 thus pointing to a $(Cu^{+} + In^{3+}) \leftrightarrow 2Zn^{2+}$ coupled substitution. In stannite, the atomic concentrations of In, Cu, and Sn yield negative correlations at In + Cu = 2 and In + Sn = 1. The incorporation of In in the structure of these two minerals can be contextualized in the sphalerite–stannite–roquesite pseudoternary system.

The availability of Cu during the crystallization of sphalerite is necessary for In enrichment in sphalerite. In this study, the highest values of In in sphalerite were found in the Diez vein in the Siete Suyos mine; the sphalerite richest in In occurs as micrometer-sized crustiform micro-bands that are also enriched in Cu, and that contain local chalcopyrite disease texture that is suggestive of a high activity of Cu in the mineralizing fluids.

Our analytical results point to the identification of intermediate-sulfidation state assemblages with abundant sphalerite and stannite as the chief host for In in the Ánimas–Chocaya–Siete Suyos district and probably in other similar, dome-hosted Bolivian-type deposits.

Supplementary Materials: Available online at www.mdpi.com/xxx/s1. Table S1: List of samples. Table S2: Representative EMPA analyses.

Author Contributions: Conceptualization, L.T., J.C.M., P.A. and O.R.A.-B.; fieldwork, L.T., M.Caz., J.C.M., L.G., D.A., B.T., A.M., D.M.; methodology, L.T., M.Caz., J.C.M., M.T., M.Cam.; writing—original draft preparation, L.T., M.Caz.; writing—review and editing, A.C., J.C.M., P.A., O.R.A.-B.

Funding: This study benefitted from the Peruvian CONCYTEC-FONDECYT-World Bank project 107-2018-FONDECYT-BM-IADT-AV, the budged granted by the Generalitat de Catalunya (Autonomous Government of Catalonia) to the Consolidated Research Group SGR 444 and the AECID project A3/042750/11.

Acknowledgments: The help and hospitality extended by the miners from the Ánimas and Siete Suyos cooperatives during sampling and field work are most gratefully acknowledged. We appreciate the technical support by Xavier Llovet (Centres Científics i Tecnològics, Universidad de Barcelona, CCiT-UB) during the acquisition of EPMA data. We appreciate constructive comments from two anonymous reviewers, which have helped us to improve the manuscript.

Conflicts of Interest: The authors declare no conflict of interest. The funders had no role in the design of the study; in the collection, analyses, or interpretation of data; in the writing of the manuscript, or in the decision to publish the results.

References

1. Jorgenson, J.D.; George, M.W. Mineral Commodity Profile: Indium. *U.S. Geological Survey Open-File Report 2004-1300*. 2004. Available online: https://pubs.usgs.gov/of/2004/1300/2004-1300.pdf (accessed on 3 December 2018).
2. Bleiwas, D.I. Byproduct mineral commodities used for the production of photovoltaic cells. *Us Geol. Surv. Circ.* **2010**, *1365*, 1–10. Available online: http://pubs.usgs.gov/circ/1365 (accessed on 30 April 2019).
3. Skirrow, R.G.; Huston, D.L.; Mernagh, T.P.; Thorne, J.P.; Dulfer, H.; Senior, A.B. *Critical Commodities for a High-Tech World: Australia's Potential to Supply Global Demand*; Geoscience Australia: Canberra, Australia, 2013.
4. Kesler, S.E.; Simon, A.C. *Mineral Resources, Economics and the Environment*, 2nd ed.; Cambridge University Press: Cambridge, UK, 2015; pp. 243–244.
5. Sykes, J.P.; Wright, J.P.; Trench, A.; Miller, P. An assessment of the potential for transformational market growth amongst the critical metals. *Appl. Earth Sci.* **2016**, *125*, 21–56.
6. European Commission. Critical Raw Materials. Available online: https://ec.europa.eu/growth/sectors/raw-materials/specific-interest/critical_en (accessed on 5 July 2018).
7. Frenzel, M.; Mikolajczak, C., Reuter, M.A.; Gutzmer, J. Quantifying the relative availability of high-tech by-product metals—The cases of gallium, germanium and indium. *Resour. Policy* **2017**, *52*, 327–335.

8. Shanks, W.C.P., III; Kimball, B.E.; Tolcin, A.C.; Guberman, D.E. Germanium and indium. In *Critical Mineral Resources of the United States—Economic and Environmental Geology and Prospects for Future Supply*; Schulz, K.J., DeYoung, J.H., Jr., Seal, R.R., II, Bradley, D.C., Eds.; U.S. Geological Survey Professional Paper; U.S. Geological Survey: Reston, VA, USA, 2017; pp. I1–I27. doi:10.3133/pp1802I.
9. Werner, T.T.; Mudd, G.M.; Jowitt, S.M. The world's by-product and critical metal resources part III: A global assessment of indium. *Ore Geol. Rev.* **2017**, *86*, 939–956.
10. Avarmaa, K.; Klemettinen, L.; O'Brien, H.; Taskinen, P.; Jokilaakso, A. Critical metals Ga, Ge and in: Experimental evidence for smelter recovery improvements. *Minerals* **2019**, *9*, 367.
11. Schwarz-Schampera, U.; Herzig, P.M. *Indium: Geology, Mineralogy and Economics*; Springer: Heidelberg, Germany, 2002.
12. Cook, N.J.; Ciobanu, C.L.; Pring, A.; Skinner, W.; Shimizu, M.; Danyushevsky, L.; Saini-Eidukat, B.; Melcher, F. Trace and minor elements sphalerite: A LA-ICPMS study. *Geochim. Cosmochim. Acta* **2009**, *73*, 4761–4791.
13. Cook, N.J.; Ciobanu, C.; Williams, T. The mineralogy and mineral chemistry of indium in sulphide deposits and implications for mineral processing. *Hydrometallurgy* **2011**, *108*, 226–228.
14. Schwarz-Schampera, U. Indium. In *Critical Metals Handbook*, 1st ed.; Gunn, G., Ed.; American Geophysical Union and Wiley: Chichester, UK, 2014; pp. 204–229.
15. Ohta, E. Occurrence and chemistry of indium-containing minerals from the Toyoha Mina, Hokkaido, Japan. *Min. Geol.* **1989**, *39*, 355–372.
16. Shimizu, T.; Morishita, Y. Petrographic, chemistry and near-infrared microthermometry of indium-bearing sphalerite from the Toyoha polymetallic deposit, Japan. *Econ. Geol.* **2012**, *107*, 723–735.
17. Frenzel, M.; Hirsch, T.; Gutzmer, J. Gallium, germanium, indium and other trace and minor elements in sphalerite as a function of deposit type—A meta-analysis. *Ore Geol. Rev.* **2016**, *76*, 52–78.
18. Bauer, M.E.; Seifert, T.; Burisch, M.; Krause, J.; Richter, N.; Gutzmer, J. Indium-bearing sulfides from the Hämmerlein skarn deposit, Erzgebirge, Germany: Evidence for late-stage diffusion of indium into sphalerite. *Min. Depos.* **2019**, *54*, 175–192.
19. Bauer, M.E.; Burisch, M.; Ostendorf, J.; Krause, J.; Frenzel, M.; Seifert, T.; Gutzmer, J. Trace element geochemistry of sphalerite in contrasting hydrothermal fluid systems of the Freiberg district, Germany: Insights from LA-ICP-MS analysis, near-infrared light microthermometry of sphalerite-hosted fluid inclusions, and sulfur isotope geochemistry. *Min. Depos.* **2019**, *54*, 237–262.
20. Pavlova, G.G.; Palessky, S.V.; Borisenko, A.S.; Vladimirov, A.G.; Seifert, T.; Phan, L.A. Indium in cassiterite and ores of tin deposits. *Ore Geol. Rev.* **2015**, *66*, 99–113.
21. Ivanov, V.V.; Rodionov, D.A.; Tarkhov, Y.A. Character of the distribution and the average content of indium in some mineral from deposits of various genetic types. *Gechemistry* **1963**, *11*, 1056–1067.
22. Benzaazoua, M.; Marion, P.; Pinto, A.; Migeon, G.; Wagner, F.E. Tin and indium mineralogy within selected samples from the Neves Corvo ore deposit (Portugal): A multidisciplinary study. *Min. Eng.* **2003**, *16*, 1291–1302.
23. Carvalho, J.R.S.; Relvas, J.M.R.S.; Pinto, A.M.M.; Frenzel, M.; Krause, J.; Gutzmer, J.; Pacheco, N.; Fonseca, R.; Santos, S.; Caetano, P.; et al. Indium and selenium distribution in the Neves-Corvo deposit, Iberian Pyrite Belt, Portugal. *Miner. Mag.* **2018**, *82*, 5–41.
24. Ye, L.; Cook, N.J.; Ciobanu, C.L.; Yuping, L.; Qian, Z.; Tiegeng, L.; Wei, G.; Yulong, Y.; Danyushevskiy, L. Trace and minor elements in sphalerite from base metal deposits in South China—A LA-ICPMS study. *Ore Geol. Rev.* **2011**, *39*, 188–217.
25. Moura, M.A.; Botelho, N.F.; Carvalho de Mendonça, F. The indium-rich sulfides and rare arsenates of the Sn-In-mineralized Mangabeira A-type granite, central Brazil. *Can. Miner.* **2007**, *45*, 485–496.
26. Cook, N.J.; Sundblad, K.; Valkama, M.; Nygård, R.; Ciobanu, C.L.; Danyushevsky, L. Indium mineralization in A-type granites in southeastern Finland: Insights into mineralogy and partitioning between co-existing minerals. *Chem. Geol.* **2011**, *284*, 62–73.
27. Shimizu, M.; Kato, A. Roquesite-bearing tin ores from the Omodani, Akenobe, Fukoku, and Ikuno polymetallic vein-type deposits in the inner zone of Southwestern Japan. *Can. Miner.* **1991**, *29*, 207–215.
28. Jovic, S.M.; Guido, D.M.; Melgarejo, J.C.; Páez, G.N.; Ruiz, R.; Schalamuk, I.B. The indium-bearing minerals of the Pingüino polymetallic vein system, Deseado massif, Patagonia, Argentina. *Can. Miner.* **2011**, *49*, 931–946.

29. Murakami, H.; Ishihara, S. Trace elements of indium-bearing sphalerite from tin-polymetallic deposits in Bolivia, China and Japan: A femto-second LA-ICPMS study. *Ore Geol. Rev.* **2013**, *53*, 223–243.
30. Liu, J.; Rong, Y.; Zhang, S.; Liu, Z.; Chen, W. Indium Mineralization in the Xianghualing Sn-Polymetallic Orefield in Southern Hunan, Southern China. *Minerals* **2017**, *7*, 173.
31. Liu, J. Indium Mineralization in a Sn-Poor Skarn Deposit: A Case Study of the Qibaoshan Deposit, South China. *Minerals* **2017**, *7*, 76.
32. Sahlström, F.; Arribas, A.; Dirks, P.; Corral, I.; Chang, Z. Mineralogical distribution of germanium, gallium and indium at the Mt Carlton high-sulfidation epithermal deposit, NE Australia, and comparison with similar deposits worldwide. *Minerals* **2017**, *7*, 213.
33. Torres, B.; Melgarejo, J.C.; Torró, L.; Camprubí, A.; Castillo-Oliver, M.; Artiaga, D.; Campeny, M.; Tauler, E.; Jiménez-Franco, A.; Alfonso, P.; et al. The Poopó Polymetallic Epithermal Deposit, Bolivia: Mineralogy, Genetic Constraints, and Distribution of Critical Elements. *Minerals* **2019**, *9*, 472.
34. Soler, P. Variations des teneurs en elements mineurs (Cd, In, Ge, Ga, Ag, Bi, Se, Hg, Sn) des minerais de Pb-Zn de Ia province polymetallique des Andes du Perou Central. *Min. Dep.* **1987**, *22*, 135–143.
35. Benites, D.; Torró, L.; Vallance, J.; Quispe, P.; Sáez, J.; Rosas, S.; Fernández-Baca, A.; Gamarra, J.; Camprubí, A.; Fontboté, L. Ore mineralogy of the In-bearing Ayawilca Zn-Ag-Sn-Cu project, Pasco, Peru. In *Life with Ore Deposits on Earth, Proceedings of the 15th Biennial Meeting of the Society for Geology Applied to Mineral Deposits, Glasgow, Scotland, 27–30 August 2019*; University of Glasgow Publicity Services: Glasgow, Scotland, 2019; pp. 1681–1684.
36. Paar, W.H.; de Brodtkorb, M.K.; Sureda, R.J.; Topa, D. A microprobe study of complex Ag-Sn ores from Pirquitas, Jujuy province, Argentina. In Proceedings of the Abstracts for the Plenary Lectures, Symposia, and Special Sessions of the 17th General Meeting of the International Mineralogical Association, Toronto, Japan, 7–19 August 1998; p. A118.
37. Ishihara, S.; Murakami, H.; Marquez-Zavalia, M.F. Inferred indium resources of the Bolivian tin-polymetallic deposits. *Resour. Geol.* **2011**, *61*, 174–191.
38. Jiménez-Franco, A.; Alfonso, P.; Canet, C.; Trujillo, J.E. Mineral chemistry of In-bearing minerals in the Santa Fe mining district, Bolivia. *Andean Geol.* **2018**, *45*, 410–432.
39. Torró, L.; Melgarejo, J.C.; Gemmrich, L.; Mollinedo, D.; Cazorla, M.; Martínez, A.; Pujol-Solà, N.; Farré- de-Pablo, J.; Camprubí, A.; Artiaga, D.; et al. Spatial and temporal control on the distribution of indium in xenothermal vein-deposits: The Huari Huari district, Potosí, Bolivia. *Minerals* **2019**, *9*, 304.
40. Ahlfeld, F.; Schneider-Scherbina, A. *Los Yacimientos Minerales y de Hidrocarburos de Bolivia*; Ministerio de Minas y Petróleo: La Paz, Bolivia, 1964; pp. 1–388.
41. Cacho, A.; Melgarejo, J.C.; Camprubí, A.; Torró, L.; Castillo-Oliver, M.; Torres, B.; Artiaga, D.; Tauler, E.; Martínez, A.; Campeny, M.; et al. Mineralogy and Distribution of Critical Elements in the Sn-W-Pb-Ag-Zn Huanuni Deposit, Bolivia. *Minerals* **2019**, submitted.
42. Sempere, T. *Phanerozoic Evolution of Bolivia and Adjacent Regions*; American Association of Petroleum Geologists (AAPG): Tulsa, OK, USA,1995; Volume 62, pp. 207–230.
43. Sempere, T.; Hérail, G.; Oller, J.; Bonhomme, M.G. Late Oligocene-Early Miocene major tectonic crisis and related basins in Bolivia. *Geology* **1990**, *18*, 946–949.
44. Lamb, S.; Hoke, L.; Kennan, L.; Dewey, J. Cenozoic evolution of the Central Andes in Bolivia and northern Chile. *Geol. Soc. Spec. Publ.* **1997**, *121*, 237–264.
45. Suarez-Soruco, R. *Compendio de Geología de Bolivia*; Servicio Nacional de Geología y Minería, Yacimientos Petrolíferos Fiscales Bolivianos: Cochabamba, Bolivia, 2000; pp. 39–76.
46. Eichelberger, N.; McQuarrie, N.; Ryan, J.; Karimi, B.; Beck, S., Zandt, G. Evolution of crustal thickening in the central Andes, Bolivia. *Earth Planet. Sci. Lett.* **2015**, *426*, 191–203.
47. Morgan, G.B.; London, D.; Luedke, R.G. Petrochemistry of Late Miocene perluminous silicic volcanic rocks from the Morococala field, Bolivia. *J. Petrol.* **1998**, *4*, 601–632.
48. Jiménez, N.; López-Velásquez, S.; Magmatism in the Huarina belt, Bolivia, and its geotectonic implications. *Tectonophysics* **2008**, *459*, 85–106.
49. Ishihara, S. The granitoid series and mineralization. *Econ. Geol.* **1981**, 458–484, doi:10.5382/AV75.14.
50. Lehmann, B.; Ishihara, S.; Michel, H.; Miller, J.; Rapela, C.; Sanchez, A.; Tistl, M.; Winkelmann, L. The Bolivian tin province and regional tin distribution in the Central Andes: A reassessment. *Econ. Geol.* **1990**, *85*, 1044–1058.

51. Murray, B.P.; Horton, B.K.; Matos, R.; Heizler, M.T. Oligocene-Miocene basin evolution in the northern Altiplano, Bolivia: Implications for evolution of the central Andean backthrust belt and high plateau. *Geol. Soc. Am. Bull.* **2010**, *122*, 1443–1462.
52. Maffione, M.; Speranza, F.; Faccenna, C. Bending of the Bolivian orocline and growth of the central Andean plateau: Paleomagnetic and structural constraints from the Eastern Cordillera (22–24° S, NW Argentina). *Tectonics* **2009**, 28, TC4006.
53. Clark, A.H.; Farrar, E.; Caelles, J.C.; Haynes, S.J.; Lortie, R.B.; McBride, S.L.; Quirt, G.S.; Robertson, R.C.R.; Zentilli, M. Longitudinal variations in the metallogenetic evolution of the central Andes: A progress report. *Geol. Assoc. Can. Spec. Pap.* **1976**, *14*, 23–58.
54. Sillitoe, R.H. Andean mineralization: A model for the metallogeny of convergent plate margins. *Geol. Assoc. Can. Spec. Pap.* **1976**, *14*, 59–100.
55. Sillitoe, R.H. Musings on future exploration targets and strategies in the Andes. *Econ. Geol.* **2004**, 11, 1–14.
56. Mlynarczyk, M.S.J.; Williams-Jones, A.E. The role of collisional tectonics in the metallogeny of the Central Andean tin belt. *Earth Planet. Sci. Lett.* **2005**, *240*, 656–667.
57. Wörner, G.; Schildgen, T.F.; Reich, M. The Central Andes: Elements of an Extreme Land. *Elements* **2018**, *14*, 225–230.
58. Wörner, G.; Mamani, M.; Blum-Oeste, M. Magmatism in the Central Andes. *Elements* **2018**, *14*, 237–244.
59. Fontboté, L. Ore Deposits in the Central Andes. *Elements* **2018**, *14*, 257–261.
60. Heuschmidt, B.; Bellot de la Torre, J.; Miranda Angles, V.; Claure Zapata, M. Las Areas Prospectivas de Bolivia para yacimientos metalíferos. *Boletín Del. Serv. Nac. De Geol. Y Min.* **2002**, *30*, 1–154.
61. Arce-Burgoa, O. *Metalliferous Ore Deposits of Bolivia*, 2nd ed.; SPC Impresores: La Paz, Bolivia, 2009; pp. 1–233.
62. Sillitoe, R.H.; Halls, C.; Grant, J.N. Porphyry tin deposits in Bolivia. *Econ. Geol.* **1975**, *70*, 913–927.
63. Turneaure, F.S. The Bolivian tin-silver province. *Econ. Geol.* **1971**, *66*, 215–225.
64. Cunningham, C.G.; Zartman, R.E.; McKee, E.H.; Rye, R.O.; Naeser, C.W.; Sanjinés, O.; Ericksen, G.E.; Tavera, F. The age and thermal history of Cerro Rico de Potosi, Bolivia. *Min. Depos.* **1996**, *31*, 374–385.
65. Kempe, U.; Lehmann, B.; Wolf, D.; Rodionov, N.; Bombach, K.; Schwengfelder, U.; Dietrich, A. U-Pb SHRIMP geochronology of Th-poor, hydrothermal monazite: An example from the Llallagua tin-porphyry deposit. *Geochim. Cosmochim. Acta* **2008**, *72*, 4352–4366.
66. Kelly, W.C.; Turneaure, F.S. Mineralongy, paragenesis and geothermometry of the tin and tungsten deposits of the Eastern Andes, Bolivian. *Econ. Geol.* **1970**, *65*, 609–680.
67. Sillitoe, R.H.; Steele, G.B.; Thompson, J.F.H.; Lang, J.R. Advanced argillic lithocaps in the Bolivian tin-silver belt. *Min. Depos.* **1998**, *33*, 539–546.
68. Phillipson, S.E.; Romberger, S.B. Volcanic stratigraphy, structural controls, and mineralization in the San Cristobal Ag-Zn-Pb deposit, southern Bolivia. *J. S. Am. Earth Sci.* **2004**, *16*, 667–683.
69. Sugaki, A.; Ueno, H.; Shimada, N.; Kusachi, I.; Kitakaze, A.; Hayashi, K.; Kojima, S.; Sanjines, O.; Sanches, A.; Veralde, O. Geological study on the polymetallic ore deposits in the Quechisla district, Bolivia. *Sci. Rep. Tohoku Univ. Ser. 3* **1983**, *15*, 409–460.
70. MacFadden, B.J.; Anaya, F.; Swisher, C.C., III. Neogene paleomagnetism and oroclinal bending of the central Andes of Bolivia. *J. Geophys. Res.* **1995**, *100*, 8153–8167.
71. Lamb, S.; Hoke, L. Origin of the high plateau in the Central Andes, Bolivia, South America. *Tectonics* **1997**, *16*, 623–649.
72. Kamenov, G.; MacFarlane, A.W.; Riciputi, L. Sources of lead in the San Cristobal, Pulacayo, and Potosí Mining Districts, Bolivia, and reevaluation of ore lead isotope provinces. *Econ. Geol.* **2002**, *97*, 573–592.
73. Grant, J.N.; Halls, C.; Avila, W.; Snelling, N.J. K-Ar ages of igneous rocks and mineralization in part of the Bolivian tin belt. *Econ. Geol.* **1979**, *74*, 838–851.
74. Buerger, M.J.; Maury, J.L. Tin ores of Chocaya, Bolivia. *Econ. Geol.* **1927**, *22*, 1–13.
75. Ramdohr, P. *The Ore Minerals and Their Intergrowths*, 3rd ed.; El Sevier: Amsterdam, The Netherlands, 1969; p. 1192.
76. Einaudi, M.T. The intermediate product of pyrrhotite alteration. *Am. Miner.* **1971**, *56*, 1297–1302.
77. Oen, I.S.; Kager, P.; Kieft, C. Oscillatory zoning of a discontinuous solid-solution series: Sphalerite-stannite. *Am. Miner.* **1980**, *65*, 1220–1232.
78. Schorr, S.; Hoebler, H.-J.; Tovar, M. A neutron diffraction study of stannite—kësterite solid solution series. *Eur. J. Miner.* **2007**, *19*, 65–73.

79. Clark, A.H. Stability field of monoclinic pyrrhotite. *Inst. Min. Met. Trans. Sec. B* **1966**, *75*, 232–235.
80. Kretschmar, U.; Scott, S.D. Phase relations involving arsenopyrite in the system Fe-As-S and their application. *Can. Miner.* **1976**, *14*, 364–386.
81. Rottier, B.; Kouzmanov, K.; Wälle, M.; Bendezú, R.; Fontboté, L. Sulfide replacement processes revealed by textural and LA-ICP-MS trace element analyses: Example from the early mineralization stages at Cerro de Pasco, Peru. *Econ. Geol*. **2016**, *111*, 1347–1367.
82. Scott, S.D.; Barnes, H.L. Sphalerite geothermometry and geobarometry. *Econ. Geol.* **1971**, *66*, 653–669.
83. Chocaya-Animas (Animas-Chocaya). Available online: https://www.mindat.org/loc-262154.html (accessed on 30 September 2019).
84. Einaudi, M.T.; Hedenquist, J.W.; Inan, E.E. Sulfidation state of fluids in active and extinct hydrothermal systems: Transitions from porphyry to epithermal environments. *Soc. Econ. Geol. Spec. Publ.* **2003**, *10*, 285–313.
85. Sillitoe, R.H.; Hedenquist, J.W. Linkages between volcanotectonic settings, ore-fluid compositions, and epithermal precious metal deposits. *Geol. S. Am.* **2003**, *10*, 314–343.
86. Camprubí, A.; Albinson, T. Epithermal deposits in México—An update of current knowledge, and an empirical reclassification. In *Geology of México: Celebrating the Centenary of the Geological Society of México*; Alaniz-Álvarez, S.A., Nieto-Samaniego, A.F., Eds.; *Geol. S. Am.* **2007**, *422*, 377–415.
87. Parasyuk, O.V.; Voronyuk, S.V.; Gulay, L.D.; Davidyuk, G.Y.; Halka, V.O. Phase diagram in the of the CuInS-ZnS system and some physical properties of solid solutions phases. *J. Alloys Compd.* **2003**, *348*, 57–64.
88. Schorr, S.; Wagner, G. Structure and phase relations of the Zn[2x](CuIn)[1 − x]S [2] solid solution series. *J. Alloys Compd.* **2005**, *396*, 202–207.
89. Johan, Z. Indium and germanium in the structure of sphalerite: An example of coupled substitution with copper. *Min. Pet.* **1988**, *39*, 211–229.
90. Cook, N.J.; Ciobanu, C.L.; Brugger. J.; Etschmann, B.; Howard, D.L.; de Jonge, M.D.; Ryan, C.; Paterson, D. Determination of the oxidation state of Cu in substituted Cu-In-Fe-bearing sphalerite via μ-XANES spectroscopy. *Am. Miner.* **2012**, *97*, 476–479.
91. Kojima, S.; Nagase, T.; Inoue, T.A. Coprecipitation experiment on the chalcopyrite disease texture involving Fe-bearing sphalerite. *J. Miner. Petrol. Econ. Geol.* **1995**, *90*, 261–267.

© 2019 by the authors. Licensee MDPI, Basel, Switzerland. This article is an open access article distributed under the terms and conditions of the Creative Commons Attribution (CC BY) license (http://creativecommons.org/licenses/by/4.0/).